Lab on a Chip

PAPER

View Article Online
View Journal | View Issue

Cite this: *Lab Chip*, 2023, **23**, 3016

Modular droplet injector for sample conservation providing new structural insight for the conformational heterogeneity in the disease-associated NQO1 enzyme†

Diandra Doppler, [ab] Mukul Sonker, [ab] Ana Egatz-Gomez, [ab] Alice Grieco,[c] Sahba Zaare,[bd] Rebecca Jernigan,[ab] Jose Domingo Meza-Aguilar,[b] Mohammad T. Rabbani,[ab] Abhik Manna, [ab] Roberto C. Alvarez,[bd] Konstantinos Karpos,[bd] Jorvani Cruz Villarreal, [ab] Garrett Nelson,[bd] Jay-How Yang,[ab] Jackson Carrion,[ab] Katherine Morin,[ab] Gihan K. Ketawala,[ab] Angel L. Pey, [e] Miguel Angel Ruiz-Fresneda, ‡[c] Juan Luis Pacheco-Garcia, [f] Juan A. Hermoso, [c] Reza Nazari,[bd] Raymond Sierra,[g] Mark S. Hunter,[g] Alexander Batyuk, [g] Christopher J. Kupitz,[g] Robert E. Sublett,[g] Stella Lisova,[g] Valerio Mariani,[g] Sébastien Boutet,[g] Raimund Fromme, [ab] Thomas D. Grant,[h] Sabine Botha,[bd] Petra Fromme,[ab] Richard A. Kirian, [bd] Jose Manuel Martin-Garcia *[c] and Alexandra Ros *[ab]

Droplet injection strategies are a promising tool to reduce the large amount of sample consumed in serial femtosecond crystallography (SFX) measurements at X-ray free electron lasers (XFELs) with continuous injection approaches. Here, we demonstrate a new modular microfluidic droplet injector (MDI) design that was successfully applied to deliver microcrystals of the human NAD(P)H:quinone oxidoreductase 1 (NQO1) and phycocyanin. We investigated droplet generation conditions through electrical stimulation for both protein samples and implemented hardware and software components for optimized crystal injection at the Macromolecular Femtosecond Crystallography (MFX) instrument at the Stanford Linac Coherent Light Source (LCLS). Under optimized droplet injection conditions, we demonstrate that up to 4-fold sample consumption savings can be achieved with the droplet injector. In addition, we collected a full data set with droplet injection for NQO1 protein crystals with a resolution up to 2.7 Å, leading to the first room-temperature structure of NQO1 at an XFEL. NQO1 is a flavoenzyme associated with cancer, Alzheimer's and Parkinson's disease, making it an attractive target for drug discovery. Our results reveal for the first time that residues Tyr128 and Phe232, which play key roles in the function of the protein, show an unexpected conformational heterogeneity at room temperature within the crystals. These results suggest that different substates exist in the conformational ensemble of NQO1 with functional and mechanistic implications for the enzyme's negative cooperativity through a conformational selection mechanism. Our study thus demonstrates that microfluidic droplet injection constitutes a robust sample-conserving injection method for SFX studies on protein crystals that are difficult to obtain in amounts necessary for continuous injection, including the large sample quantities required for time-resolved mix-and-inject studies.

Received 1st March 2023,
Accepted 26th May 2023

DOI: 10.1039/d3lc00176h

rsc.li/loc

[a] *School of Molecular Sciences, Arizona State University, Tempe, AZ, 85287-1604, USA. E-mail: alexandra.ros@asu.edu*
[b] *Center for Applied Structural Discovery, The Biodesign Institute, Arizona State University, Tempe, AZ, 85287-7401, USA*
[c] *Department of Crystallography and Structural Biology, Institute of Physical Chemistry Blas Cabrera, Spanish National Research Council (CSIC), Serrano 119, 28006, Madrid, Spain. E-mail: jmmartin@iqfr.csic.es*
[d] *Department of Physics, Arizona State University, Tempe, AZ, 85287-1504, USA*
[e] *Departamento de Química Física, Unidad de Excelencia en Química Aplicada a Biomedicina y Medioambiente e Instituto de Biotecnología, Universidad de Granada, Av. Fuentenueva s/n, 18071, Granada, Spain*
[f] *Departamento de Química Física, Universidad de Granada, Av. Fuentenueva s/n, 18071 Granada, Spain*
[g] *Linac Coherent Light Source (LCLS), SLAC National Accelerator Laboratory, Menlo Park, 94025 CA, USA*
[h] *Department of Structural Biology, Jacobs School of Medicine and Biomedical Sciences, SUNY University at Buffalo, 955 Main St, Buffalo, NY, 14203, USA*

† Electronic supplementary information (ESI) available. See DOI: https://doi.org/10.1039/d3lc00176h

‡ Present address: Departamento de Microbiología, Universidad de Granada, Av. Fuentenueva s/n, 18071 Granada, Spain.

Introduction

With nearly 205 000 structures deposited in the Protein Data Bank (PDB) as of April 2023, protein X-ray crystallography has become one of the most successful structural biology techniques since the first three-dimensional structure of a protein, myoglobin, was revealed. Insulin's mechanism of action[1] mass production of penicillin,[2] understanding sickle cell anemia,[3] the structure of DNA,[4] and HIV inhibitors,[5,6] are just a few of the many world-changing discoveries made possible by X-ray crystallography.[7,8] Advancements in crystallography were enabled through technological improvements in sample handling such as the use of cryoprotectant mother liquors[9] to mitigate radiation damage and produce macromolecular structures at sub-zero temperature,[10] and sealed crystal holders, oils, and humidified environments to slow down dehydration and prolong measurement times.[11] The development of bright X-ray radiation sources such as 3rd generation synchrotrons and hard X-ray free electron lasers (XFELs) has made it possible to determine structures of very weakly-diffracting biomacromolecular crystals at room temperature.[12] These two X-ray sources are, however, characterized by significant differences in pulse duration, peak brilliance, and repetition structure and therefore require the development of different approaches to sample handling.[13]

With the increased availability of XFELs over the past 10 years, serial femtosecond crystallography (SFX) methods have been developed to obtain room-temperature structural information from crystals that are too small, weakly scattering, or radiation damage-sensitive to be probed at synchrotrons.[14,15] In SFX, each crystal is typically exposed only once because the intense, ultrashort XFEL pulse triggers a cascade of ionization events that ends with the crystal exploding. However, as atomic motions of protein molecules inside crystals are slower than the duration of an XFEL pulse, diffraction patterns can be recorded on the detector before structure-altering radiation damage becomes apparent.[16,17] Since each diffraction pattern only measures partial Bragg reflection intensities at a single random orientation, few thousands of crystals are needed to collect a complete data set.[18]

XFELs generate femtosecond pulses at repetition rates in the range of 60 Hz to 4.5 MHz. Pulse repetition structures can be complex; for example, the European XFEL (EuXFEL) generates 10 X-ray pulse trains per second, with each train currently consisting of as many as 352 pulses spaced about 900 ns apart.[19] An example of a simpler pulse structure is the evenly spaced 120 pulse per second train at the Linac Coherent Light Source (LCLS) XFEL,[20] which will be increased up to 1 MHz for LCLS-II in the future. A major drawback of SFX experiments at XFELs is the large amount of sample required in most instances. It can often take from months to years to produce protein crystals that are suitable for SFX experiments, and the resulting protein crystals are often more precious than diamonds.[21] The choice of sample delivery method is thus crucial for the success of SFX experiments. An ideal sample delivery method must: 1) replenish crystals in the interaction region ideally at the same rate of the XFEL pulses;[15] 2) consider sample characteristics such as crystal size and morphology, fragility, and concentration; and 3) fulfill seemingly incompatible requisites, such as the need to work in vacuum to avoid background scatter from air, while preventing the sample from drying, freezing, or clogging.[22]

The two most important metrics that should be considered when deciding on which sample injection system to use for a given experiment are the "hit rate" and "delivery efficiency". The hit rate is defined as the fraction of XFEL pulses that produce a useful diffraction pattern (*e.g.*, one with Bragg reflections). The delivery efficiency is defined as the number of useful diffraction patterns generated per sample quantity (*e.g.*, hits per μL of solution for known protein concentrations or crystal density). Defined in this way, delivery efficiency is dependent on hit rate, and one might additionally define the "geometric efficiency" as the fraction of the sample volume that is exposed to X-rays. An ideal injector has a geometric efficiency close to 1, a sample hit rate that depends on the stability of the injection set-up and sample quality (also close to 1), and a delivery efficiency that additionally depends on crystal size and density (it can exceed 1 to account for multiple crystals interacting with the X-ray beam in a single shot). However, a number of complications must be considered, such as the effect of sample exchange on hit rate, the effect of sample-loading dead volumes on delivery efficiency, and the effects of gas or liquid background signals on the ultimate signal-to-noise ratio of the measurement.

Sample delivery methods roughly fall into three categories: injection methods, fixed-target methods, and hybrid combinations of these two methods.[22] Methods based on injection deliver a thin stream of a crystal slurry that intersects the XFEL beam in either vacuum or helium and air atmospheres, typically using a gas dynamic virtual nozzle (GDVN).[23,24] However, the major drawback of jet injection is the fact that most crystals are never hit by the X-rays, with most of the sample wasted in between pulses, so that a complete dataset may require up to several hundred milligrams of crystallized protein. This is multiplied with each time point to be measured in mix-and-inject time-resolved (TR) crystallography experiments, where each time point requires the same amount of protein crystals to obtain a full data set.[25–28]

Double flow focusing nozzles (DFFN),[29] and co-flow of oil and aqueous sample injection[30] have been developed to reduce the sample consumption, stabilize the flow, and reduce evaporative cooling in vacuum. In addition, viscous media injectors have been developed to create extremely low flow rates and reduce sample consumption significantly, though these are not fast enough to replenish crystals at MHz repetition rate XFELs.[31–34] Low flow rates for sample conservation during continuous liquid injection were also

induced using an electrospinning principle with the MESH injector[35,36] at the expense of higher background when crystal slurries are probed in the electro-spun cone[37] instead of the jet due to experimental optimizations of hit rates and potential impact on crystal structures.

In fixed-target methods, the crystal suspension is loaded onto the surface of a solid support that is rastered through the interaction region of the X-ray beam. These devices use thin layers of materials such as silicon,[38,39] cycloolefin-copolymer (COC),[40,41] polydimethylsiloxane (PDMS),[42] COC/PDMS combinations,[43] polyethylene terephthalate,[44] graphene layers in combination with polymers,[45] and polyimide.[46] Typically, fixed-target devices enable high hit rates (10–40%) compared to the lower hit rates (1–10%) frequently achieved with continuous liquid delivery systems.[47–50] However, despite the high sample hit rate, fixed-target devices usually require the use of more than one device for a complete data set and require time-intensive procedures to load each device and/or exchange with the previous one (particularly for data collection in vacuum) during beamtimes. Evaporation during data collection can be problematic, and MHz repetition frequencies can hardly be achieved. Fixed targets also affect data processing when the devices cause non-uniform and/or systematically varying background due to misalignment with the 'windows' of the target, and residual salt traces from sample loading can result in additional diffraction spots.

To address the unmet needs of lowering sample consumption with liquid crystal injectors, droplet-based injection methods have been recently developed. Aqueous sample droplets can be generated *via* piezoelectric[51] or acoustic[52] effects referred to as droplet-on-demand techniques.[53] They allow droplet generation to match the pulse structures of current XFELs.[54] However, drop-on-demand techniques are inherently limited by clogging effects through settling crystals and are currently incompatible with vacuum conditions. To overcome these limitations, we developed the use of segmented droplet generation, where crystal laden droplets are generated through sheering at a microfluidic intersection segmented by an immiscible oil.[55,56] We demonstrated successful droplet injection for SFX experiments by solving the first room-temperature structure of the 3-deoxy-D-manno-octulosonate 8-phosphate synthase (KDO8PS) protein at the EuXFEL.[57] We further developed this approach to match the 120 Hz repetition rate of the LCLS with a capillary-coupled version of the droplet injector.[58] Here, we have designed a fully 3D-printed modular droplet injector (MDI) that integrates all necessary injector components, but with a significantly reduced footprint (about an order of magnitude in injector length) to ease the use of the injector in various XFEL experimental chambers. In addition, we have demonstrated the integration of the droplet injection with electrical triggering feedback control into the data stream at the MFX instrument at LCLS. This new capability allows for on-the-fly optimization of droplet injection parameters in order to maximize crystal hit rates.

We demonstrate the successful use of the MDI for the proteins phycocyanin and the human NQO1 (NAD(P)H: quinone oxidoreductase 1). We show that our injector reduces sample consumption by a factor of three to four and for the latter, we determined the first room-temperature SFX structure at 2.7 Å resolution. NQO1 is a flavoenzyme essential for the antioxidant defense system, stabilization of tumor suppressors, and the NAD(P)H-dependent two-electron reduction of a wide variety of substrates, including the activation of quinone-based chemotherapeutics.[59–61] In addition, alterations in NQO1 function are associated with cancer, Alzheimer's and Parkinson's disease, which makes this enzyme an attractive target for drug discovery.[62] Our results reported here provide important insight into the conformational heterogeneity of the human NQO1, highlighting the high plasticity of this enzyme in the catalytic site and hence shed light on the molecular basis of NQO1 functional cooperativity.

Materials and methods

Materials

Perfluorodecalin (PFD) and 1*H*,1*H*,2*H*,2*H*-perfluoro-1-octanol (perfluorooctanol, PFO) were purchased from Sigma-Aldrich, USA. SU-8 developer was obtained from Microchem, USA. Deionized water (18 MΩ) was supplied from a LA755 Elga purification system (Elga Lab water, USA) and isopropyl alcohol (IPA) and ethanol were obtained from VWR Analytical (USA) and Decon Labs (USA), respectively. Fused silica capillaries (360 μm outer diameter, 100 μm inner diameter) were purchased from Molex, USA. Hardman extra-fast setting epoxy was purchased from All-Spec, USA. Conducting silver epoxy was purchased from M.G. Chemicals Ltd., Canada, and insulated copper wire from Remington Industries, USA. *E. coli* BL21 (DE3) competent cells were purchased from Agilent Technologies (USA). Yeast extract and tryptone were purchased from Condalab (Madrid, Spain). EDTA-free protease inhibitor cocktail, isopropyl β-D-1-thiogalactopyranoside (IPTG), ampicillin, sodium phosphate, sodium chloride, imidazole, flavin adenine dinucleotide (FAD), sodium acetate, K-HEPES, and Tris-HCl were purchased from Merck (Madrid, Spain). Polyethylene glycol (PEG) 3350 was purchased from Hampton Research (USA).

Modular droplet injector design and fabrication

All components of the modular injection device were designed and fabricated as previously described.[57] Briefly, the devices were designed in Fusion 360 (AutoDesk, USA) or AutoCAD (AutoDesk, USA), 3D-printed with a Photonic Professional GT 3D-printer (Nanoscribe GmbH, Germany) using IP-S photoresist (Nanoscribe GmbH, Germany), developed in SU-8 developer, and rinsed in IPA.

The injection device consisted of three 3D-printed components: a droplet generator, a droplet detector, and a gas-dynamic virtual nozzle (GDVN)[63,64] (Fig. 1). Studs and receptacles on the top and bottom of the corresponding

pieces were added to connect the three components. In the first component, droplets were generated at the 45° intersection of a central and a lateral channel (cross-section 100 μm × 100 μm). Two channels (350 μm × 100 μm × 50 μm) were included parallel to the main channel, separated from the droplet-generating junction by 5 μm and filled with conducting silver epoxy-filled electrodes. Each electrode was connected *via* a nickel-chrome wire inserted in the conductive channel and soldered to a 2 m copper wire insulated with enamel and the connection was sealed with heat-shrink tubing. The second component was an optical fiber detector holder, with a central channel for segmented liquid flow and two axial openings to fit and align the tips of two optical fiber cables. An auxiliary channel was wrapped around the droplet detector to facilitate connecting the gas line to the GDVN. The third component was the GDVN, as previously described.[58]

A 1.5 m long fused silica capillary was inserted into each of the droplet generator inlets and the detector holder gas line inlet and fixed using epoxy. After the capillaries were fully cured in place, the three components were joined together by plugging in the studs and receptacles and applying the epoxy. A fully assembled MDI device is depicted in Fig. 1(c).

Fluidic operation and setup

Oil and crystal sample were loaded in custom stainless-steel reservoirs with plungers driven by high pressure liquid chromatography (HPLC) pumps (LC20AD, Shimadzu Co., Japan) with water as the hydraulic fluid. SLI-0430 and SLG-0075 (Sensirion, Switzerland) liquid-flow sensors were situated in the water lines upstream of the reservoirs. The pumps, sensors, and reservoirs were connected using PEEK tubing (Zeus, USA, 250 μm ID and 1/16 in OD) with fittings and ferrules from IDEX Health & Science LLC (USA).

Throughout experiments at LCLS at the Macromolecular Femtosecond Crystallography (MFX) instrument, devices were mounted on a custom-made bracket provided by LCLS and installed in the Helium-Rich Ambient (HERA) chamber. The chamber helium pressure was regulated by a high-pressure gas valve (Proportion-air, USA). The capillaries, detector fibers, and insulated wires were fed through ports at the side of the chamber. Reservoirs containing the protein crystals were mounted on a modified version of a previous anti-settler device.[65] The outlets of the oil and protein sample reservoirs were connected to the droplet generator *via* the assembled 100 μm inner diameter fused silica capillaries.

Droplet detector

The droplet detector was realized with a 1470 nm, 5 mW, single mode (SM), SC/FC terminated pigtailed laser diode (QPhotonics, USA) as the light beam source, as previously described.[58] Single-mode bendable optical fiber (EZ_Bend, OFS, USA) and multi-mode (MM) optical fiber (ClearCurve, Corning, USA), both terminated with 1 mm outer-diameter custom zirconia ferrules (OZ Optics, Canada), were used for light delivery and collection, respectively. The ferrule-terminated patches were plugged into opposite sides of the 3D-printed detector holder to transversely illuminate and collect the light transmitted through the droplet detector holder channel. The refractive index and absorbance differences between the oil and aqueous droplets, as well as the droplet geometry, produced variations in the transmitted light intensity that was measured using a photodetector (ADAFC4, ThorLabs, USA).

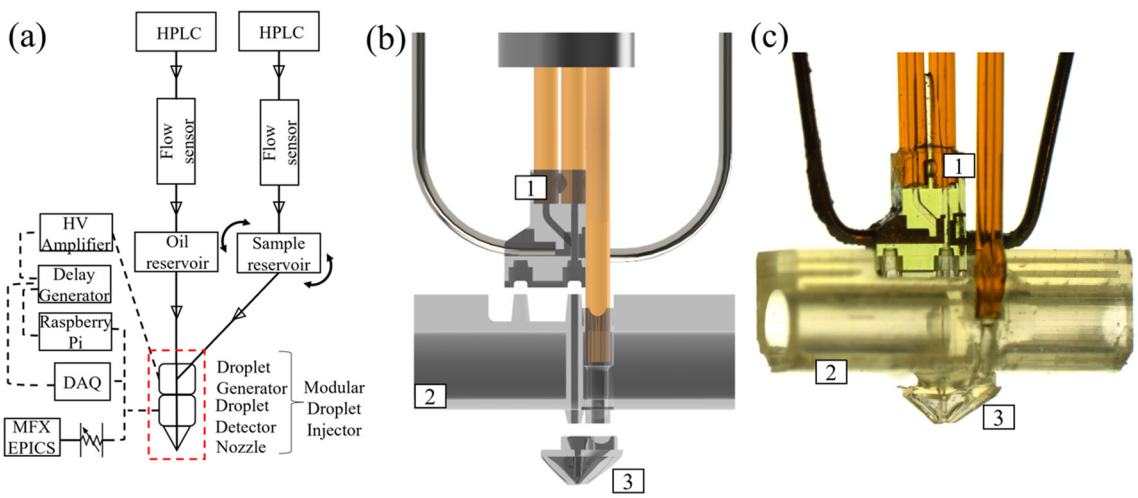

Fig. 1 (a) Schematic set-up of the MDI and control hardware (not to scale) implemented at the MFX instrument. (b) Graphic of the three MDI components: 1) droplet generator, 2) droplet detector, 3) 3D-printed GDVN. Three silica capillaries (orange) deliver the oil/sample solutions and the GDVN sheathing gas. The NiCr wires (black) attached to the droplet generator allow electrical droplet stimulation. (c) A microscopic image of the MDI fully assembled with the same components as in (b).

Droplet shape analysis

The droplet shape and assessment of crystal content were analyzed for two systems of buffer-only and crystal-containing buffer droplets. The droplet detector signal was analyzed off-line using a custom MatLAB code that tallied the absolute and local droplet minima past a set threshold. We quantified the signal variation between droplets with and without crystals, for 10 minutes (~72 000 droplets) for each condition and analyzed the number of local minima in each aqueous signal segment.

Feedback mechanism

The droplet frequency and phase control were implemented using a Raspberry Pi microcomputer (Model B, Raspberry Pi Foundation, UK) outfit with a voltage measurement DAQ hat (MCC 118, Digilent Inc., USA), a digital delay generator (DG645, Stanford Research Systems, US), a high voltage amplifier (Model 2210, Trek Inc., USA), and a Powerlab data acquisition system (8/35, AD Instruments, US). The droplet signal from the photodetector was analyzed concurrently with data collection using custom Python scripts applied to the Raspberry Pi, to diagnose the droplet frequency and the timing of the leading edge relative to the XFEL reference pulse. The script then calculated required parameter adjustments needed to maintain the leading edge at the desired position and applied them to the digital delay generator that drives the droplet electrical trigger. This feedback system allows for a fixed delay between the droplets and the XFEL reference over long measurement times. During XFEL experiments, a custom attenuator was used to feed the photodetector signal into the digitizer (DC282, Acqiris, Switzerland) for droplet signal recording through the MFX Experimental Physics and Industrial Control System (EPICS) system.

Phycocyanin isolation and crystallization

Cubic microcrystals of phycocyanin were grown on-site in the LCLS Biolabs at the Arrillaga Science Center (ASC) at SLAC National Laboratory (CA, USA). In brief, phycocyanin was isolated from the thermophilic cyanobacterium *Thermosynechococcus elongatus* as follows: the cells (50 g) were harvested from 100 L cell culture by tangential filtration and then disrupted using a microfluidizer (Microfluidics Model M110-L). After differential centrifugation to remove unbroken cells, the photosynthetic membranes were washed 4 times as described in Gisriel *et al.*[66] The third mixture of supernatant was used for isolation of phycocyanin. Phenylmethylsulfonyl fluoride (PMSF) was freshly added to the supernatant to serve as protease inhibitor (87 mg PMSF were dissolved in 1 mL of DMSO and 400 μL of this stock were added to 400 mL of supernatant). The solution was clarified from the remaining thylakoid membranes by ultracentrifugation using a Ti45-rotor (Beckman, USA) with centrifugation at 45 000 rpm at 4 °C for 1 hour. The supernatant was carefully removed and filtered through 0.2 μm filter cups (VWR Analytical, USA). Subsequently, the phycocyanin was further purified by ion exchange chromatography on a Q-Sepharose HP column and equilibrated with buffer A, which was comprised of 30 mM HEPES pH 7.0. A gradient of buffer B (30 mM HEPES pH 7.0, 200 mM $MgCl_2$) was passed through the column with phycocyanin eluting at a concentration of 75 mM $MgCl_2$. Absorbance spectra (260–700 nm) were collected from all peak fractions including the fraction that contained pure phycocyanin (absorption maximum at 620 nm) and were free of allophycocyanin contamination (indicated by a shoulder peak at 650 nm) as well as other protein contamination (indicated by a 620 nm to 280 nm ratio >4). All batches were pooled and concentrated to 50 mg mL^{-1} using 15 mL Millipore spin concentrators with molecular weight cut-offs at 50 kDa. The concentrated protein was frozen in 100 μL aliquots at −80 °C and shipped frozen to the LCLS.

Once onsite, phycocyanin was crystallized using the batch method in sets of 100 μL protein plus 100 μL precipitant. A small stir bar was added to the 500 μL reaction vessel with the 100 μL protein solution (50 mg mL^{-1}) in buffer containing 30 mM HEPES pH 7.0 and 75 mM $MgCl_2$. The protein was stirred at 200 rpm and 100 μL of precipitant solution (25% PEG 3350 in 30 mM HEPES and 75 mM $MgCl_2$) were added in 16 steps with a 15 second time delay between steps. Crystals of 5–15 μm grew overnight at RT. For injection purposes, most phycocyanin batches were produced by resuspending the settled crystals in the crystallization solution (12.5% PEG 3350 in 30 mM HEPES and 75 mM $MgCl_2$). Each crystallization experiment thereby yielded 200 μL of crystal suspension for sample delivery. Eight crystallization batches were combined and filtered through a 20 μm stainless steel frit with a PEEK ring (IDEX Health & Science LLC, USA) before being loaded into 1.5 mL sample reservoirs. The final injection buffer varied in PEG 3350 content from 12.5 to 18%.

NQO1 purification and crystallization

Protein expression and purification of human NQO1 were carried out as previously described[67] with some modifications. Briefly, *Escherichia coli* BL21 (DE3) cells were transformed with pET46 Ek/LIC plasmid containing the cDNA of human NQO1 and grown overnight in 800 mL of lysogeny broth supplemented with 0.1 mg mL^{-1} ampicillin (LBA) at 37 °C. This starter culture was diluted in 4 L of fresh LBA and grown at 37 °C until the optical density at 600 nm reached values between 0.6 and 0.8. Expression was then triggered by the addition of IPTG at a final concentration of 0.5 mM. Induced cells were further incubated for 4 h at 28 °C, harvested by centrifugation, resuspended in 40 mL of binding buffer (BB: 20 mM sodium phosphate, 300 mM NaCl and 50 mM imidazole at pH 7.4) containing 1 mM PMSF, flash frozen in liquid N_2, and stored at −80 °C. The following day, cells were lysed by sonication (3 cycles of 2 min each, alternating 2 s ON/2 s OFF with 2 min rest on ice). The lysate was cleared by centrifugation at 30 000 rpm at 4 °C for 40

min. The supernatant containing NQO1 was filtered through 0.45 μm filters and subsequently loaded onto an immobilized Ni^{2+} affinity chromatography column (Thermo Scientific™ HisPur™ Ni-NTA resin), which was previously equilibrated with BB. After collecting the flowthrough, the column was washed with 20 column volumes (CVs) of BB and eluted with 10 CVs of elution buffer (BB containing 500 mM imidazole). The eluted protein was dialyzed against 50 mM K-HEPES at pH 7.4. NQO1 protein was further purified by size-exclusion chromatography (SEC) using a HiLoad 16/600 Superdex 200 prep grade (GE Healthcare) using 20 mM K-HEPES, 200 mM NaCl at pH 7.4 containing FAD at a final concentration of 1 mM. Pure protein was concentrated to a final concentration of 20 mg mL^{-1} using 30 kDa concentrators from Millipore, flash frozen and stored at −80 °C. The purity and integrity of the protein were checked by SDS-PAGE.

Prior to the SFX experiment, initial crystallization trials were carried out using both the batch and the free interface diffusion methods[68] from previously reported crystallization conditions[69] for large crystals as reference. Microcrystals of the human NQO1 were obtained on-site in the LCLS Biolabs at the Arrillaga Science Center (ASC) at SLAC National Laboratory (CA, USA) by the batch with agitation method as follows: in a 3 mL glass vial, 100 μL of the protein solution at 25 mg mL^{-1} were slowly added dropwise to 300 μL of the precipitant solution (0.1 M Tris pH 8.5, 0.2 M sodium acetate, 20% polyethylene glycol (PEG) 3350, and 20 μM FAD) while stirring at 200 rpm. Upon addition of the protein, the solution turned turbid immediately and needle-shaped crystals of dimensions 10 × 2 × 2 μm^3 grew at room temperature in about 6 h. This original crystal suspension was spun down at 150 rpm, 25% of the supernatant was removed, and the pellet was resuspended in the remaining volume prior to loading into a sample reservoir. Sample A and B resulted from two different crystallization batches, but were otherwise similar. A schematic of the crystallization set-up and the NQO1 microcrystals is illustrated in Fig. S-1.†

Data collection and structure determination

NQO1 and phycocyanin SFX data were collected at the MFX instrument at LCLS during beamtime LW79 using the MDI device presented in this study. Diffraction snapshots were recorded on the ePix10k detector[70] at an X-ray energy of 9.6 keV using a pulse duration of 40 fs. The sample-to-detector distance was 86.3 mm. A customized version of OM (OnDA (Online Data Analysis) Monitor)[71] was used for live feedback of crystal and droplet hit rates based on X-ray scattering.[58] In addition to X-ray scattering analysis, OM integrated data from the optical droplet detection system described above. This integration enabled visualization of the correlation between optical droplet detection and X-ray interaction with droplets and crystal diffraction. For the structure solution of NQO1, a total of 1 533 276 frames were collected, of which 10 269 were classified as hits by the Cheetah software.[72] A more stringent hit-finding procedure within CrystFEL identified 7598 hits. About 48% of the identified hits could be indexed, giving rise to a total of 4317 indexed lattices. The Bragg reflections were integrated using the software package CrystFEL[73] (version 0.10.1) after indexing was attempted with CrystFEL's indexamajig using the algorithms XGANDALF,[74] MOSFLM[75] and DIRAX,[76] in that order. The intensities were converted to structure factor amplitudes using AIMLESS (from the CCP4 suite package[77]), and a fraction of 5% reflections were included in the generated R_{free} set. Phasing was performed using molecular replacement with PHASER[78] using the PDB code 1DXQ[79] as the search model. The obtained model was refined using alternate cycles of automated refinement with REFMAC5[80] and manual inspection was performed with COOT.[81]

The same hit finding and indexing procedure was applied for the case of phycocyanin, with 625 979 frames collected, and an initial number of 9257 hits identified with CHEETAH. CrystFEL retained 8172 of these hits, of which 5216 were successfully indexed giving rise to individual 7465 crystal lattices. The structure was solved and refined as described previously.[82]

All data collection and refinement statistics of both proteins are summarized in Table S-2.† All figures of the NQO1 structure presented in this manuscript were generated with PYMOL.[83] The final refined structures were validated using the PDB Validation Service and submitted to the Protein Data Bank for deposition with PDB 8C9J (NQO1) and 8FWA (phycocyanin).

Results and discussion

Segmented droplet generation with the ultimate goal to significantly reduce sample waste in SFX experiments was previously demonstrated with the structure of the enzyme KDO8PS at the SPB/SFX instrument at the EuXFEL in a vacuum chamber[57] and more recently with KDO8PS and lysozyme crystals at the MFX instrument at LCLS.[58] Here, we focus on improvements to four important aspects to segmented droplet injection: droplet generation, droplet detection, jetting the crystal-laden droplets into the XFEL path, and a system for synchronizing the droplet arrival to the region of interaction with the beam and the XFEL pulses. We present a single, fully 3D-printed modular droplet injection (MDI) device, with an order-of-magnitude smaller footprint than our previous design. In the MDI, the droplets are generated at less than 3 mm from the nozzle orifice, with advantages for droplet synchronization discussed later in this manuscript (Fig. 1). The droplet generation software and hardware have been re-designed to incorporate a synchronization control strategy for the electrically stimulated droplet release and to fulfill the requisites of the LCLS MFX instrument, where these advancements have been applied to NQO1 and phycocyanin protein injection and serial crystallography.

MDI design and droplet detector characteristics

A schematic representation of the MDI experimental setup is shown in Fig. 1(a), and the employed experimental setup is

depicted in Fig. S-2.† Oil and sample are displaced using HPLC pumps from steel reservoirs into capillaries leading to the y-shaped droplet generator, where crystal-laden droplets segmented by oils are formed at a natural frequency governed by the employed flow rates. The droplets then flow through the droplet detector into the GDVN and are jetted into the XFEL path. The droplet generator, detector, and nozzle components are depicted in Fig. 1(b) and (c). The three pieces have interlocking studs and receptacles for adjoining the pieces into the final device assembly. The geometry and placement of these elements have been carefully optimized through several iterations to the final design shown in Fig. 1(b) and (c). The distance from the droplet generation to the GDVN opening is 2.5 mm, much shorter than in our previous capillary coupled devices (>10 mm).[58] Given the mechanically noisy environment of the XFEL, generating the droplets as close as possible to the GDVN is key to maintaining synchronization between droplets and X-ray pulses.

The new MDI design integrates the fiber-optic droplet detector, a critical element for diagnosing the droplet generation frequency and the feedback loop control applied for droplet synchronization with the XFEL pulses. In contrast to our previous realization of this detector,[58] the fibers are inserted in a high-resolution 3D-printed holder section. This allows for high-precision positioning of the optical fibers relative to the fluid channel integrated in the optical fiber holder, while connecting the droplet generator at the top, and the nozzle at the bottom. The microfluidic channel in the fiber holder directly receives the generated segmented droplet/oil liquid without the need for interconnecting capillaries. The close proximity of the three printed MDI elements minimizes the distance the droplets travel before reaching the GDVN, which helps maintain synchronization and spatial overlap between the X-ray pulses and crystal-laden droplets. In addition, the new droplet detector holder design required a unique solution to attach the fused silica capillary delivering He gas to the GDVN for jetting. Since the fused silica capillary is too stiff to be attached to the small footprint GDVN, a channel transporting He to the GDVN was created at the periphery of the droplet detector holder (see Fig. 1(b) and (c)).

Droplet detection is based on refractive index differences between oil and aqueous buffer droplets from an incident 1470 nm wavelength laser beam transmitted through an optical fiber. The walls of the central channel transporting the droplets are 100 μm thick, leading to insignificant attenuation of the signal as determined with a power meter.[58] The droplet signal shape and intensity can occasionally vary between various detector holders and runs. These variations can be ascribed to the manual insertion of fibers, in-house fiber termination with custom ferrules (see Materials and methods section for details), and differences between the 3D printed devices. The assembly was still rigid enough to allow for reliable droplet detection, while the signal intensity differences were compensated by adjusting the laser intensity and the sensitivity of the photodetector.

Crystal-laden droplets produce droplet detection signals that differ significantly from buffer-only droplets, which can be used as a valuable diagnostic tool, as demonstrated in Fig. 2(a–d). Aqueous droplets appear as valleys in the detector signal since the transmittance of aqueous solutions is lower than that of the oil at 1470 nm. These valleys are often bound by sharp peaks caused by refraction at the moving oil/sample interface, with an intensity and slope that depends sensitively on droplet geometry and composition. The signal corresponding to aqueous buffer-only droplets appears as a fairly smooth, reproducible trace. In contrast, the crystal-laden droplets produce irregular ripple patterns in the corresponding signal. This contrast for droplets generated with and without crystals is shown in Fig. 2(a and b) and (c and d) for NQO1 and phycocyanin, respectively. The signal ripple is caused by the laser beam absorption and refraction due to variable numbers of protein crystals with different shapes and sizes. The signals for droplets containing NQO1 or phycocyanin crystals showed twice as many minima than the signal for buffer-only droplets (Fig. 2(e)) assessed on ~72 000 droplets per condition, where the minima in the buffer-only droplets are due only to the leading and ending edges of the droplet. The protein NQO1 forms needle-shaped crystals with a large aspect ratio (typically 10 × 2 × 2 μm^3), while phycocyanin forms cubic crystals (with sides around 20 μm). Regardless of the crystal shape and size, however, the signal variation for crystal-containing droplets was significantly larger than for buffer-only droplets, which served as an excellent diagnostic to verify that the crystals were transported in droplets to the GDVN for injection into the path of the XFEL.

Droplet generation and injection performance

Droplet release in the droplet generator was electrically triggered to improve droplet synchronization with the pulsed XFEL. The MDI droplet generator is located a few mm above the interaction region of the jet with the XFEL beam. This distance varies due to the manual assembly of the devices and XFEL beam alignment. The droplet signal measured at the MDI was fed into a control loop to correct for any spatial variations, and therefore adjust the timing of the crystal-containing droplet arrival to the region of interaction with the XFEL beam. A custom Python script applied through a Raspberry Pi was used to compare the occurrence of the leading edge of the droplet signal and the XFEL reference signal. The calculated time difference was used to adjust the timing of the droplet electrical stimulation, to produce and maintain a user-defined optimal droplet edge position, ϕ_s. The script updated the delay generator parameters (amplitude, duration, and delay) every 120 droplets. The output pulse from the delay generator was then amplified 100 times and sent to the electrodes within the droplet generator to stimulate the droplet release. The electrodes in the MDI droplet generator region are shown in Fig. 1(c) for reference.

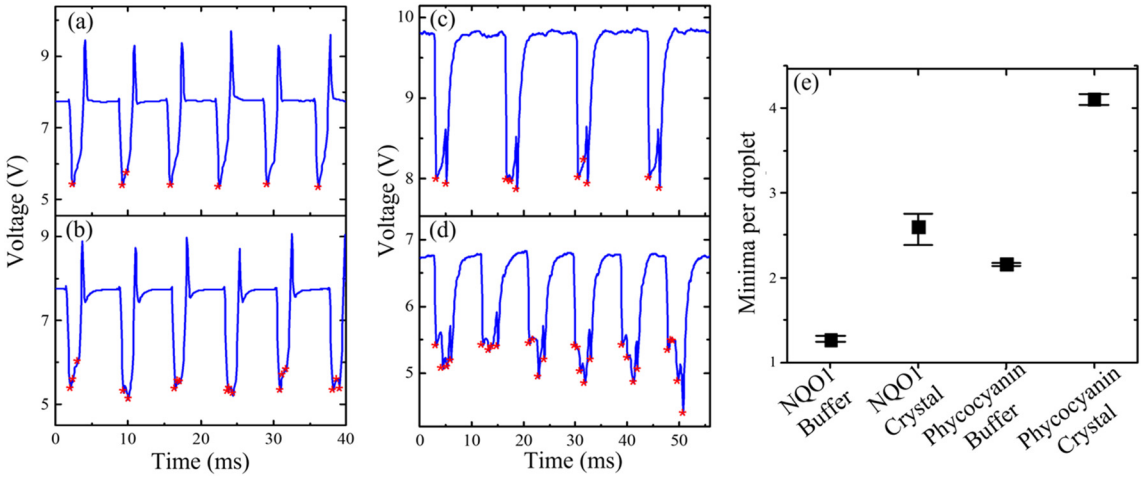

Fig. 2 Droplet detector voltage output for (a) NQO1 buffer-only droplets, (b) NQO1 crystal-containing buffer droplets, (c) phycocyanin buffer-only droplets, and (d) phycocyanin crystal-containing droplets where the red stars indicate the local minima. (e) Comparison of local minima per droplet for buffer-only and crystal-containing droplets for NQO1 and phycocyanin.

The successful implementation of the feedback mechanism was demonstrated with the injection of NQO1 and phycocyanin crystal laden droplets (Fig. 3(a) and (b), respectively). The waterfall representation consists of heat plots of the droplet detector signal stacked at 8.3 ms intervals, where the start and end of each stacked line correspond to one period of the XFEL reference, *i.e.*, the time between X-ray pulses. The waterfall plot provides an intuitive graphical representation of the droplet phase delay, ϕ_s, marked in red relative to the XFEL reference. The applied electrical stimulation timing (phase) and duration are shown as white bars overlapped on the waterfall plots. In Fig. 3(a) and (b), the electrical stimulus duration was 1 ms with an amplitude of 50 and 150 V, respectively. The intensity of the electrical stimulus was experimentally adjusted until the minimum voltage that produced the desired effect in the droplet frequency was found, which varied with the buffer composition. During the representative waterfall plot for NQO1 crystals shown in Fig. 3a, the feedback control was programmed to produce ϕ_s of 3.5 ms between the XFEL reference and the leading edge of the droplet. Fig. 3(b) depicts a waterfall plot for injected phycocyanin crystals, where the target droplet edge position was set to 2 ms for the first two min, and then changed to 4 ms for the remaining 8 min.

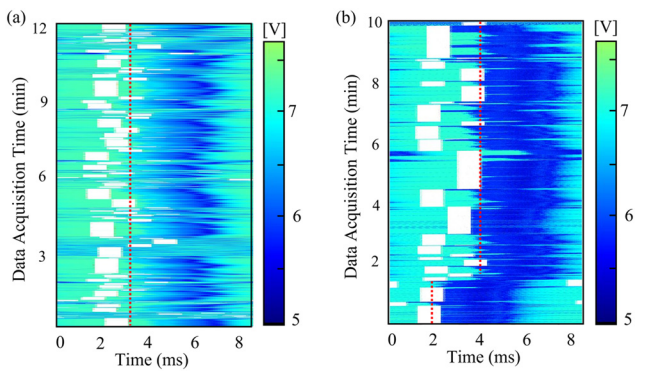

Fig. 3 A characteristic waterfall plot depicting the background of oil in teal, the protein crystal-containing droplet in deep blue, the trigger signal in white, and ϕ_s as a red dashed line for continuously triggered and locked-in droplets at 120 Hz for (a) NQO1 and (b) phycocyanin during LW79 at the MFX instrument.

A further improvement to previous segmented droplet injection[58] constitutes the integration of the droplet feedback mechanism with the LCLS data acquisition system to capture the droplet traces through a high-speed digitizer. Integration into the EPICS data stream enabled droplet injection diagnostic comparisons to metrics such as the crystal hit rate and the correlation of programmed ϕ_s to droplet hit rates, which were visualized with OM. Droplet hit rates provide a measure of synchronization between droplet arrival at the point of intersection with the XFEL beam pulse through assessment of the scattering differences between oil and sample, as previously described.[58] To further optimize the synchronization of the droplets with the XFEL using the EPICS interface, an automated parameter scan was realized with a custom Python script to rapidly and reproducibly adjust the droplet triggering conditions until maximal crystal diffraction was collected.

We investigated the electrical stimulation parameters including the duration and amplitude of the electrical stimulus, and the ability to reproducibly align the leading edge of the droplet to a pre-set ϕ_s with this parameter scan tool. Fig. 4 illustrates droplet signal traces stacked as waterfall plots resulting from parameter sweeps during NQO1 (Fig. 4(a) and (c) and phycocyanin Fig. 4(b)) injection. The data acquisition was limited to only the first 6.3 ms of the 8.3 ms XFEL period due to the digitizer properties. Fig. 4(a) illustrates a sweep where the target phase between the droplet leading edge and the XFEL reference was set to 1, 3, 5, and 7 ms, each maintained for 3 min, using a 1 ms long

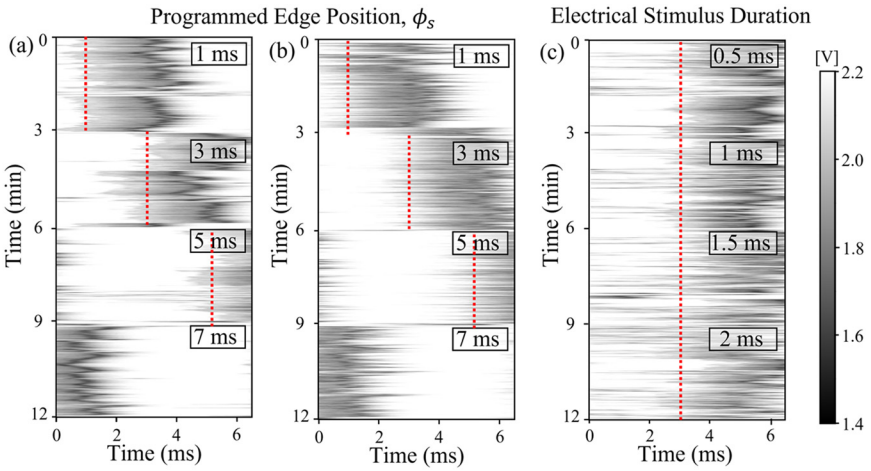

Fig. 4 Examples for parameter sweeps to diagnose the droplet injection conditions: (a) the leading droplet edge position was changed from 1 to 7 ms in 2 ms steps, each being recorded for a 3 min run. The injected sample was NQO1. (b) as in (a), but the sample was phycocyanin. (c) The trigger duration was changed across 4 runs for NQO1 from 0.5 ms to 2 ms in steps of 0.5 ms. The greyscale color bar represents the amplitude of the droplet signal in volts and the red dotted line ϕ_s.

and 70 V electrical trigger pulse while NQO1 was injected in droplets. Evidently, the leading edges of the droplets within the 8.3 ms XFEL period align as per the programmed delay. For 5 and 7 ms, the leading edge follows the programmed ϕ_s; however, the droplet appears wrapped around the XFEL reference because the droplet signal overlaps and extends beyond the next XFEL reference.

We further investigated the capability of shifting the leading edge of the droplet in reference to the XFEL pulses with phycocyanin crystals (Fig. 4(b)). For this sample, an amplitude of 130 V and a 1.5 ms duration was used for the electrical stimulus while performing a stepwise sweep of programmed target droplet leading edge of 1, 3, 5, and 7 ms each recorded during a 3 min run. As in the case of the NQO1 sample (Fig. 4(a)), the observed droplet leading edge changed according to the programmed ϕ_s. These two examples demonstrate that ϕ_s can be adjusted for different crystal samples, which is important for further optimization of droplet arrival with respect to the XFEL pulses, as discussed below.

The parameter sweep module also enables the investigation of the influence of the electrical stimulus duration. An example of this capability is shown in Fig. 4(c) with NQO1 as the sample, where the programmed electrical stimulus duration was changed from 0.5 to 2 ms in steps of 0.5 ms while keeping the desired edge position of the droplet constant at 3 ms. Additionally, Fig. S-3† shows the edge positions for the 12 minutes of droplet generation (~86 000 droplets), where the electrical stimulus duration was varied. The shorter 1 ms and 0.5 ms trigger durations provided the most stable droplet injection, with the droplet edge position most focused around the desired edge position of 3 ms.

The automated parameter sweep tool could eventually be further developed to scan other electrical stimulus parameters such as amplitude and duration, for optimized synchronization with the XFEL. As previously investigated, droplets are released by an electrical trigger-induced electrowetting effect.[55] This effect appears upon a trigger amplitude threshold, above which the droplet generation frequency stabilizes. During the LW79 beam time, the trigger amplitude was manually adjusted at the start of every run that used a new sample or a new device, using stepwise voltage increments until the droplet frequency stabilized around 120 Hz. The threshold ranged from 70 to 200 V. We ascribe this variability to the effects of the buffer conductivity and small size differences across the manually assembled devices affecting the electric field distribution.

Using the parameter sweep tool, the droplet hit rates as well as crystal hit rates could be correlated to the desired droplet leading edge position. The histogram of Fig. 5(a) depicts the number of events with a given leading-edge position in relation to the XFEL reference, measured during a programmed sweep where the target droplet leading edge was set to 1, 3, 5, and 7 ms, each setting maintained for 3 min. The frequency distribution of the measured droplet's leading-edge positions is roughly centered around the corresponding set ϕ_s, demonstrating that setting ϕ_s to a desired value results in the expected droplet position relative to the X-ray pulse to enable synchronization with the XFEL pulse scheme. Fig. 5(b) shows the crystal and droplet hit rates corresponding to the sweep in Fig. 5(a). The crystal hit rate was computed as previously described by Barty *et al.*[72] and the droplet hit rate indicates the fraction of patterns for which water solution scattering indicated the presence of the sample droplet.[58] Both the droplet and crystal hit rates were significantly larger when the programmed edge position was 3 ms for this buffer system and this particular MDI (Fig. 5(b)). We also applied this triggering parameter optimization strategy to a phycocyanin crystal sample (see Fig. S-4†). In this case, a ϕ_s of 5 ms resulted in the largest droplet and crystal hit rates, followed by ϕ_s = 3 ms. The results presented in Fig. 5 and S-4† demonstrate the success

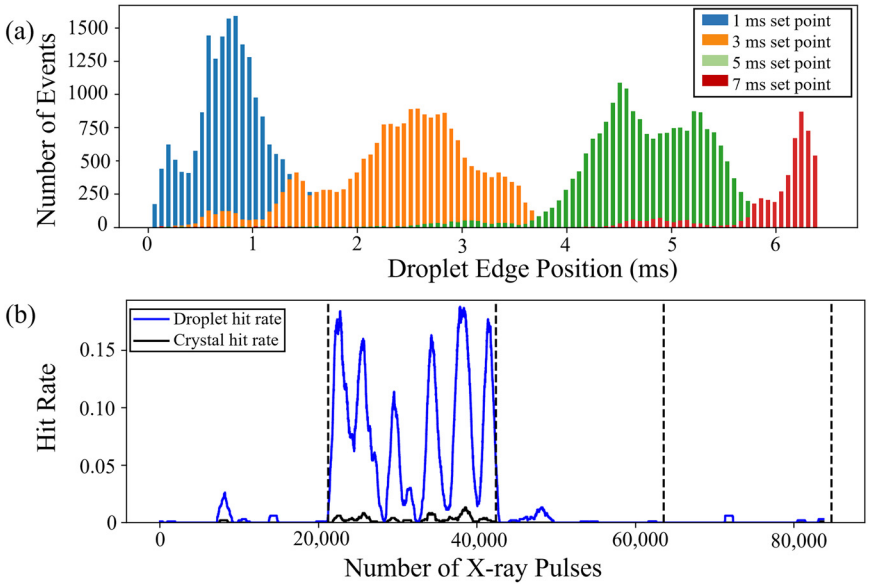

Fig. 5 Implementation of the parameter sweep for NQO1 with variation of phase delay (ϕ_s). (a) Probability of NQO1 laden droplet leading edge as obtained from a parameter sweep for 4 set-points. (b) Normalized droplet hit rate (blue) and crystal hit rate (black) during this parameter sweep for droplets containing NQO1 crystals. Patterns for each ϕ_s were 1 for 1 ms, 153 for 3 ms, 1 for 5 ms and 1 for 7 ms.

of controlling the phase of the droplet leading edge through electrically stimulated triggering as a strategy for maximization of hit rates, which can be applied to protein crystals with different crystallization and injection requirements. The triggering parameter space can be used to find optimized conditions for synchronizing the timing of the droplet arrival to the point of intersection with the XFEL pulses during droplet injection SFX experiments, including not only at the 120 Hz pulse frequency of LCLS, but also at XFELs with different pulse structures.

The parameter tool and its capabilities were tested in the last shift of the LW79 experiment, while the modular droplet injector was further characterized for several batches of NQO1 and phycocyanin and injection conditions during the preceding shifts. Tables 1 and S-1,† for NQO1 and phycocyanin, respectively, compare droplet injection with the continuous flow injection with a GDVN. While droplet generation was sustained for 6 to 12 hours over the course of one shift, these tables only summarize conditions where droplet generation and continuous flow injection were optimized for diffraction data collection.

Injection conditions for two different batches of NQO1 (sample A and B) are detailed in Table 1. For sample A, it is worth noting that the overall crystal hit rate was low when injected continuously with a GDVN, resulting in an average delivery efficiency of 9.4 indexed patterns per injected µL of sample (IP_{Sample}). When droplets were generated, but the phase delay was not optimized for droplet hits (ϕ_s = 1, 4 or 8 ms), the delivery efficiency dropped to 8.0. This is expected, since active triggering with a non-optimized phase delay can reduce the likelihood of sample being in the X-ray interaction region when the XFEL pulses arrive (potentially, the hit rate can drop to zero with an ideal injector and incorrect phase). However, Table 1 demonstrates that IP_{Sample} increases significantly when ϕ_s is programmed to 3 ms, in agreement with the parameter sweep results demonstrated above. Interestingly, when ϕ_s = 2 ms, IP_{Sample} is still high compared to GDVN injection, indicating that the optimized ϕ_s is probably in between 2 and 3 ms. We attribute this to the finite volume of the droplet, which results in a partial overlap with the XFEL pulse and therefore still results in about 3-fold higher IP_{Sample} as compared to continuous injection for the 2 ms case. We note that ϕ_s = 3 ms

Table 1 Comparison of modular droplet injection and continuous injection for two batches of NQO1 crystals

Sample	Injection method	ϕ_s (ms)	Sample flow rate (µL min^{-1})	Indexed patterns per µL	Resolution
A	Droplets	1, 4, 8	3.6	8.0	2.2 Å
	Droplets	2	3.0	28.4	
	Droplets	3	3.4	39.9	
	Droplets	4	4.0	7.5	
	GDVN	—	20	9.4	2.2 Å
B	Droplets	1, 2, 4, 5, 7	3.7	3.3	1.9 Å
	Droplets	3	3.7	9.5	
	GDVN	—	20	2.2–3.4	1.9 Å

resulted in the highest IP_{Sample}, which outperformed the continuous GDVN injection by a factor of 4. Since the droplet hit rate with the X-ray pulses was on average 7% with the optimal phase delay of 3 ms, further optimization of the injector to enhance stability and maximize droplet synchronization with the XFEL beam could yield further improvement in sample saving efficiency relative to GDVN systems. Furthermore, the highest diffraction resolution observed for NQO1 resulted in 2.2 Å for both the continuous GDVN and droplet injection for sample A, demonstrating that the droplet encapsulation in an immiscible oil phase does not affect the crystals or that the oil background contribution obscures the weaker, high-resolution reflections.

In addition, NQO1 sample B shows the same trends as sample A. When ϕ_s is optimized, there is a 3-fold increase in IP_{Sample} compared to continuous injection. In this case, IP_{Sample} is lower for the optimized phase delay; however, the diffraction resolution is higher. This could indicate that the crystals were smaller in size and potentially less concentrated than the batch of sample A.

For phycocyanin, two different sample batches (C and D) with varying PEG concentrations and thus viscosities were contrasted to GDVN injection (E) in Table S-1.† As observed with the parameter sweep (see Fig. S-4†) ϕ_s = 3 and 5 ms yielded the highest droplet and crystal hit rates. Table S-1† confirms this since a two and a 3-fold increase of IP_{Sample} over continuous injection was obtained. However, when a non-optimal ϕ_s was employed, there is still a 2-fold increase in IP_{Sample}, indicating that the droplet delay was possibly prone to more variations in the case of phycocyanin as compared to NQO1. If the droplet generation is less stable, even non-optimized droplet generation can lead to a higher IP_{Sample} as compared to the continuous GDVN injection. Furthermore, as for the NQO1 sample, phycocyanin did not result in significant changes in the diffraction resolution between the droplet-based and continuous injections. In summary, the detailed analysis presented in Tables 1 and S-1† lead to the conclusion that the sample could be conserved by up to a factor of 4 and potentially even further with optimization of droplet release and synchronization. We hypothesize that this could be achieved with improved pump instrumentation capable of enhanced flow rate stability along with the minimization of the distance between the droplet generation and the liquid jet. The sample flow rates in this work were below 5 μL min^{-1}, which would lead to a regime in which the employed GDVN was not able to generate a stable jet (data not shown). These flow rates are compatible with other injectors, such as the DFFN.[29] We point out that segmented droplet injection is favorable in SFX experiments under vacuum, while the immiscible oil phase further prolongs the injector lifetime and the length of the jets, as previously observed.[30,58]

NQO1 SFX structure

As demonstrated above, droplet injection with NQO1 crystals was successfully implemented at the MFX instrument with appropriate diagnostics, and the first room-temperature structure of the human NQO1 was solved at 2.7 Å resolution from microcrystals delivered with the modular droplet injector. Data analysis on a refined subset of data on sample B (defined above) revealed a space group of $P2_12_12_1$ with two dimers in the asymmetric unit and the following unit cell parameters: a = 61.4 Å b = 107.6 Å, c = 198.1 Å, $\alpha = \beta = \gamma = 90°$ (Fig. S-5†). Sample B was selected since it diffracted to higher resolution and the collected data was highly isomorphic (the flexibility of the MFX beamline, can lead to slight variations in the reported unit cell when adjusting the set up during data collection, such as exchanging the nozzle). Fig. 6 illustrates the two dimers in the asymmetric unit. Fig. S-6† shows a representative snapshot with diffraction up to ~2 Å resolution. The final model was refined to a 2.7 Å resolution, with final R_{work} and R_{free} of 21.1% and 24.5%, respectively. All data collection and processing parameters and statistics are presented in Table S-2.† The high quality of the NQO1 structure can be assessed from the electron $2mF_o–DF_c$ density maps shown for the catalytic site residues and the cofactor FAD (Fig. 6(b)).

Further evaluation of the NQO1 structure quality was carried out by comparing it with crystal structures reported at cryogenic conditions such as PDB entries 1D4A,[79] 1DXQ,[79] 5A4K,[84] and 5EA2.[85] Overall, all the NQO1 structures aligned very well with each other, with average root-mean-square deviation (RMSD) values of 0.378 Å for the Cα atoms. The global RMSD of 0.867 Å suggests slightly higher structural differences when the whole protein molecule is considered, mainly due to mismatch from flexible loops as well as solvent exposed regions, as one would expect.

Our structure represents the holo protein structure at room temperature, whereas the published structures were determined under cryogenic conditions with a cryo-protectant.[79,84,85] It is well known that the cryo-protectant, as well as the freezing process, can induce conformational changes that represent a narrow subset of all the possible conformations at room temperature. These differences between room-temperature and cryogenic crystallography structures have been experimentally observed for several proteins.[86–93] A careful analysis of our NQO1 structure has further revealed that residues Tyr128 and Phe232, which play a key role in the function of the protein,[94–98] show an unexpected flexibility within the crystals (Fig. 7(a)). In contrast, in all the previously reported cryogenic structures, these two residues have been typically found in a similar conformation[79,84,85] (Fig. 7(b)). The difficulty of obtaining structural and dynamic information by standard macromolecular crystallography at cryogenic conditions at synchrotrons has prevented researchers from observing this behavior from a structural perspective. Our findings offer new light on the previous reports of the two active binding sites of NQO1 acting cooperatively and displaying highly collective inter-domain and inter-monomer communication and dynamics.[98–102]

Here, we present novel SFX data showing the conformational heterogeneity of NQO1 at room temperature.

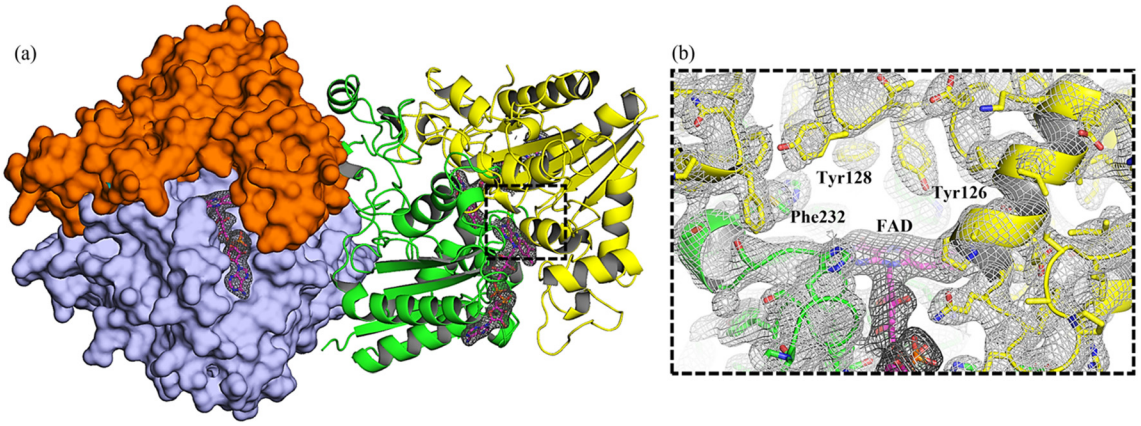

Fig. 6 SFX structure of human NQO1 obtained at MFX. (a) The two dimers of NQO1 in the asymmetric unit are depicted. The individual monomers are highlighted in green, yellow, orange, and light blue. The cofactor FAD is shown as pink sticks. The catalytic site of one of the monomers is black-boxed. (b) Closer view of the catalytic site in (a). The electron $2mF_c$–DF_o density maps at the catalytic site contoured at 1σ are shown. Residues Tyr126, Tyr128, and Phe232 which are key in the function of the enzyme are highlighted. Our results also suggest the presence of different conformational sub-states prior to NAD(P)H binding and consequent flavin reduction, thus supporting a conformational selection mechanism and providing structure–function information at high resolution.

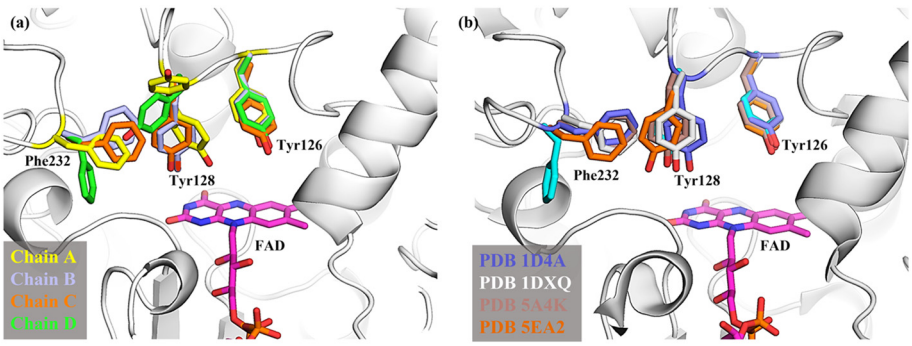

Fig. 7 (a) Superimposition of the four monomers found in the asymmetric unit of the NQO1 structure determined at MFX. Residues Tyr126, Tyr128, and Phe232, key for NQO1 function, are represented as sticks. FAD is labeled accordingly and represented as pink sticks. (b) Superimposition of the four unliganded cryogenic structures of NQO1 (PDB 1D4A,[79] PDB 1DXQ,[79] PDB 5A4K[84] and PDB 5EA2 (ref. 85)). As in (a), the key residues and FAD molecule are highlighted.

The electron density at the NQO1 catalytic site has been revealed with an extent of detail, *i.e.*, the Tyr128 and Phe232 residues (Fig. 7), up to date not unveiled by structures determined at cryogenic temperatures.[79,84,85] The conformational heterogeneity observed in our room temperature SFX structure of the human NQO1 highlights the high plasticity of this enzyme's catalytic site. Our results also suggest the presence of different conformational sub-states prior to NAD(P)H binding and consequent flavin reduction, thus supporting a conformational selection mechanism and providing structure–function information at high resolution.

Conclusion

For the first time, we demonstrate the use of a modular, fully 3D-printed droplet injector with a reduced footprint for SFX at the MFX instrument at LCLS. The droplet generation *via* electrical triggering was carefully optimized and integrated into the EPICS data recording system at the MFX instrument. Furthermore, we demonstrate how droplet injection parameters can be optimized based on the duration and amplitude of the employed electrical stimulus, but importantly, also based on the phase delay of the droplet with respect to the XFEL reference. For both NQO1 and phycocyanin, we found optimized droplet and crystal hit rates, which resulted in a larger number of indexed patterns compared to continuous GDVN injection. For NQO1, this amounted in a decrease in sample waste by a factor of four, whereas for phycocyanin, which was injected in a more viscous buffer, a 3-fold improvement was observed. Further improvement of droplet synchronization efficiency may be realized with additional stabilization of the flow rates at or below 5 μL min^{-1}. Since the droplet injection diagnostics was implemented in the data stream at MFX, segmented droplet injection holds promise to be applicable for many other protein crystal samples, not only at MFX but other XFEL instruments, including vacuum chambers, with which our

segmented droplet approach is compatible.[57] In addition to demonstrating the tunability and optimization of droplet generation for SFX at XFELs, the modular injector used in this work was successfully applied to obtain the first SFX room-temperature structure of NQO1 at 2.5 Å resolution.

NQO1 is a biomedically relevant protein that displays functional negative cooperativity.[98,99] However, there is no structural evidence describing this communication so far. Our results highlight the power of the SFX technique to describe the structure–function relationships in detail. In addition, our room temperature SFX structure highlights the high conformational heterogeneity of this enzyme in the catalytic site, and hence shed light on the molecular basis of NQO1 functional cooperativity previously described from experiments in solution.[98–101] From an equilibrium point of view, the presence of different conformational substates (with potentially different functional properties) supports that cooperative effects may arise from a conformational selection mechanism upon ligand binding.[102] Thus, understanding the NQO1 structure–function relationships and interaction with ligands (substrates and inhibitors) at the molecular level will be critical to unravel its role as an antioxidant and a potential target to treat common diseases by advancing the design of new, more potent, and effective inhibitors that can be used in the clinical realm. In the future, we also plan to perform time-resolved SFX studies in combination with the segmented droplet injector on NQO1 to investigate if the here-reported structural changes relate to functionality involved in the catalysis mechanism of the enzyme.

Author contributions

AR conceived experiments. AR, RAK, PF, DD, MS, and AEG designed experiments. DD, MS, AEG, MTR, JCV, GN, RAK, and AR contributed to device design and fabrication. SZ, KK, RA, and RAK programmed the feedback mechanism and sweeping programs. DD, MS, AEG, TDG, VM, GKK, and SeB contributed to the data analysis. AG, MARF, JLPG, ALP, and JMMG produced NQO1 protein. JHY, KM, and JC isolated the phycocyanin protein. DD, RJ, JDMA, AM, JLPG, ALP, AG, MARF, JAH, PF, CJK, and JMMG contributed to crystals sample preparation. DD, MS, AEG, RJ, JDMA, SZ, MTR, AM, RA, KK, GKK, RS, MSH, AB, CJK, RES, SL, SaB, SeB, SBo, RAK, PF, JMMG, and AR participated in the beamtime experiments either on-site or remotely. RS, MSH, AB, CJK, RES, SL, and SeB contributed to instrument set-up and experimental support and participated as beamline scientists. MARF, AG, and JMMG solved the structure of NQO1 and made all related figures. DD, AEG, MS, JMMG, and AR wrote the manuscript with input from all other co-authors.

Conflicts of interest

DD, AEG, RAK, RN, GN, MTR, AR, and MS are co-inventors on a patent related to the technology presented in this manuscript.

Acknowledgements

Financial support from the STC Program of the National Science Foundation through BioXFEL (under agreement # 1231306), ABI Innovations award (NSF # 1565180), IIBR award (# 1943448), MCB award (1817862), and the National Institutes of Health award # R01GM095583 is gratefully acknowledged. The use of the Linac Coherent Light Source (LCLS), SLAC National Accelerator Laboratory, is generously supported by the US Department of Energy, Office of Science, Office of Basic Energy Sciences under contract # DE-AC02-76SF00515. The authors would like to acknowledge the instrument group and facility staff for their assistance in the use of the MFX instrument during proposal MFXLW7919 at LCLS. The HERA system for in-helium experiments at MFX was developed by Bruce Doak and funded by the Max Planck Institute for Medical Research. This work was also supported by The Center for Structural Dynamics in Biology, NIH grant P41GM139687. Alice Grieco and Jose M. Martin-Garcia were supported by the "Ayuda de Atracción y Retención de Talento Investigador" from the Community of Madrid, Spain (REF: 2019-T1/BMD-15552). JLPG and ALP acknowledge funding from the ERDF/Spanish Ministry of Science, Innovation, and Universities—State Research Agency (grant RTI2018-096246-B-I00), Consejería de Economía, Conocimiento, Empresas, y Universidad, Junta de Andalucía (grant P18-RT-2413), and ERDF/Counseling of Economic transformation, Industry, Knowledge, and Universities (grant B-BIO-84-UGR20).

References

1 D. Crowfoot, *Nature*, 1935, **135**, 591.
2 D. C. Hodgkin, *Adv. Sci.*, 1949, **6**, 85–89.
3 J. Boyes-Watson, E. Davidson and M. F. Perutz, *Proc. R. Soc. London, Ser. A*, 1947, **191**, 83–132.
4 D. Brown, A. Michelson, A. Todd, L. Heppel, P. Whitfeld, R. Markham, R. Matthews, E. Chargaff, P. Kent, J. Lucy, G. L. Brown, M. Watson, H. Fischer, J. A. V. Butler, P. Davison, K. V. Shooter, M. Y. Khouvine, D. Hamer, D. W. F. James, R. E. Franklin, R. G. Gosling, M. H. F. Wilkins, C. W. Hooper, W. E. Seeds, A. R. Stokes, H. R. Wilson, W. E. Seeds, D. P. Riley, U. W. Arndt, B. E. Conway, D. O. Jordan, M. R. Porter, A. R. Peacocke, H. K. Schachman, K. A. Stacey, P. Alexander, J. Pouyet, C. Sadron, R. Thomas, W. G. Overend and M. Stacey, *Trans. Faraday Soc.*, 1954, **50**, 290–305.
5 J. B. Cooper, S. I. Foundling, A. Hemmings, F. E. Watson, B. L. Sibanda, T. L. Blundell, D. M. Jones, A. Hallett, B. Atrash and M. Szelke, *Biochem. Soc. Trans.*, 1987, **15**, 751–754.
6 A. Sali, B. Veerapandian, J. Cooper, S. Foundling, D. A. Hoover and T. Blundell, *EMBO J.*, 1989, **8**, 2179–2188.
7 J. M. Deisenhofer and H. Michel, *Science*, 1989, **245**, 1463–1473.
8 S. G. Rasmussen, B. T. DeVree, Y. Zou, A. C. Kruse, K. Y. Chung, T. S. Kobilka, F. S. Thian, P. S. Chae, E. Pardon, D.

Calinski, J. M. Mathiesen, S. T. Shah, J. A. Lyons, M. Caffrey, S. H. Gellman, J. Steyaert, G. Skiniotis, W. I. Weis, R. K. Sunahara and B. K. Kobilka, *Nature*, 2011, **477**, 549–555.
9 G. A. Petsko, *J. Mol. Biol.*, 1975, **96**, 381–392.
10 E. F. Garman and M. Weik, in *Protein Crystallography: Methods and Protocols*, ed. A. Wlodawer, Z. Dauter and M. Jaskolski, Springer New York, New York, NY, 2017, pp. 467–489.
11 M. Fischer, *Q. Rev. Biophys.*, 2021, **54**, 1–15.
12 J. Drenth, X-ray Sources and Detectors, *Principles of Protein X-Ray Crystallography*, Springer New York, 2017, ch. 2, pp. 21–44.
13 V. Cerantola, A. D. Rosa, Z. Konôpková, R. Torchio, E. Brambrink, A. Rack, U. Zastrau and S. Pascarelli, *J. Phys.: Condens. Matter*, 2021, **33**, 274003.
14 M. S. Hunter and P. Fromme, *X-ray Free Electron Lasers*, 2018, pp. 23–58.
15 T. R. M. Barends, B. Stauch, V. Cherezov and I. Schlichting, *Nat. Rev. Methods Primers*, 2022, **2**, 59.
16 L. Lomb, T. R. M. Barends, S. Kassemeyer, A. Aquila, S. W. Epp, B. Erk, L. Foucar, R. Hartmann, B. Rudek, D. Rolles, A. Rudenko, R. L. Shoeman, J. Andreasson, S. Bajt, M. Barthelmess, A. Barty, M. J. Bogan, C. Bostedt, J. D. Bozek, C. Caleman, R. Coffee, N. Coppola, D. P. DePonte, R. B. Doak, T. Ekeberg, H. Fleckenstein, P. Fromme, M. Gebhardt, H. Graafsma, L. Gumprecht, C. Y. Hampton, A. Hartmann, G. Hauser, H. Hirsemann, P. Holl, J. M. Holton, M. S. Hunter, W. Kabsch, N. Kimmel, R. A. Kirian, M. Liang, F. R. N. C. Maia, A. Meinhart, S. Marchesini, A. V. Martin, K. Nass, C. Reich, J. Schulz, M. M. Seibert, R. Sierra, H. Soltau, J. C. H. Spence, J. Steinbrener, F. Stellato, S. Stern, N. Timneanu, X. Wang, G. Weidenspointner, U. Weierstall, T. A. White, C. Wunderer, H. N. Chapman, J. Ullrich, L. Strüder and I. Schlichting, *Phys. Rev. B: Condens. Matter Mater. Phys.*, 2011, **84**, 214111.
17 K. Nass, A. Gorel, M. M. Abdullah, A. V. Martin, M. Kloos, A. Marinelli, A. Aquila, T. R. M. Barends, F.-J. Decker, R. Bruce Doak, L. Foucar, E. Hartmann, M. Hilpert, M. S. Hunter, Z. Jurek, J. E. Koglin, A. Kozlov, A. A. Lutman, G. N. Kovacs, C. M. Roome, R. L. Shoeman, R. Santra, H. M. Quiney, B. Ziaja, S. Boutet and I. Schlichting, *Nat. Commun.*, 2020, **11**, 1814.
18 R. Neutze, R. Wouts, D. van der Spoel, E. Weckert and J. Hajdu, *Nature*, 2000, **406**, 752–757.
19 M. Vakili, J. Bielecki, J. Knoska, F. Otte, H. Han, M. Kloos, R. Schubert, E. Delmas, G. Mills, R. de Wijn, R. Letrun, S. Dold, R. Bean, A. Round, Y. Kim, F. A. Lima, K. Dorner, J. Valerio, M. Heymann, A. P. Mancuso and J. Schulz, *J. Synchrotron Radiat.*, 2022, **29**, 331–346.
20 P. Emma, R. Akre, J. Arthur, R. Bionta, C. Bostedt, J. Bozek, A. Brachmann, P. Bucksbaum, R. Coffee, F. J. Decker, Y. Ding, D. Dowell, S. Edstrom, A. Fisher, J. Frisch, S. Gilevich, J. Hastings, G. Hays, P. Hering, Z. Huang, R. Iverson, H. Loos, M. Messerschmidt, A. Miahnahri, S. Moeller, H. D. Nuhn, G. Pile, D. Ratner, J. Rzepiela, D. Schultz, T. Smith, P. Stefan, H. Tompkins, J. Turner, J. Welch, W. White, J. Wu, G. Yocky and J. Galayda, *Nat. Photonics*, 2010, **4**, 641–647.
21 A. Löf, O. Löf and M. Ericsson, *Resource rents in the diamond industry 2014-19: Rents, issues, methods, and data availability*, Report 9292569775, WIDER Working Paper, 2021.
22 I. Martiel, H. M. Müller-Werkmeister and A. E. Cohen, *Acta Crystallogr., Sect. D: Struct. Biol.*, 2019, **75**, 160–177.
23 A. M. Gañán-Calvo, *Phys. Rev. Lett.*, 1998, **80**, 285.
24 D. DePonte, U. Weierstall, K. Schmidt, J. Warner, D. Starodub, J. Spence and R. Doak, *J. Phys. D: Appl. Phys.*, 2008, **41**, 195505.
25 G. D. Calvey, A. M. Katz, C. B. Schaffer and L. Pollack, *Struct. Dyn.*, 2016, **3**, 054301.
26 J. R. Stagno, Y. Liu, Y. R. Bhandari, C. E. Conrad, S. Panja, M. Swain, L. Fan, G. Nelson, C. Li, D. R. Wendel, T. A. White, J. D. Coe, M. O. Wiedorn, J. Knoska, D. Oberthuer, R. A. Tuckey, P. Yu, M. Dyba, S. G. Tarasov, U. Weierstall, T. D. Grant, C. D. Schwieters, J. Zhang, A. R. Ferre-D'Amare, P. Fromme, D. E. Draper, M. Liang, M. S. Hunter, S. Boutet, K. Tan, X. Zuo, X. Ji, A. Barty, N. A. Zatsepin, H. N. Chapman, J. C. Spence, S. A. Woodson and Y. X. Wang, *Nature*, 2017, **541**, 242–246.
27 M. Hejazian, C. Darmanin, E. Balaur and B. Abbey, *RSC Adv.*, 2020, **10**, 15694–15701.
28 S. Pandey, G. Calvey, A. M. Katz, T. N. Malla, F. H. M. Koua, J. M. Martin-Garcia, I. Poudyal, J.-H. Yang, M. Vakili, O. Yefanov, K. A. Zielinski, S. Bajt, S. Awel, K. Doerner, M. Frank, L. Gelisio, R. Jernigan, H. Kirkwood, M. Kloos, J. Koliyadu, V. Mariani, M. D. Miller, G. Mills, G. Nelson, J. L. Olmos, Jr, A. Sadri, T. Sato, A. Tolstikova, W. Xu, A. Ourmazd, J. C. H. Spence, P. Schwander, A. Barty, H. N. Chapman, P. Fromme, A. P. Mancuso, G. N. Phillips Jr, R. Bean, L. Pollack and M. Schmidt, *IUCrJ*, 2021, **8**, 878–895.
29 D. Oberthuer, J. Knoška, M. O. Wiedorn, K. R. Beyerlein, D. A. Bushnell, E. G. Kovaleva, M. Heymann, L. Gumprecht, R. A. Kirian, A. Barty, V. Mariani, A. Tolstikova, L. Adriano, S. Awel, M. Barthelmess, K. Dörner, P. L. Xavier, O. Yefanov, D. R. James, G. Nelson, D. Wang, G. Calvey, Y. Chen, A. Schmidt, M. Szczepek, S. Frielingsdorf, O. Lenz, E. Snell, P. J. Robinson, B. Šarler, G. Belšak, M. Maček, F. Wilde, A. Aquila, S. Boutet, M. Liang, M. S. Hunter, P. Scheerer, J. D. Lipscomb, U. Weierstall, R. D. Kornberg, J. C. H. Spence, L. Pollack, H. N. Chapman and S. Bajt, *Sci. Rep.*, 2017, **7**, 44628.
30 D. Doppler, M. T. Rabbani, R. Letrun, J. Cruz Villarreal, D. H. Kim, S. Gandhi, A. Egatz-Gomez, M. Sonker, J. Chen, F. H. M. Koua, J. Yang, M. Youssef, V. Mazalova, S. Bajt, M. L. Shelby, M. A. Coleman, M. O. Wiedorn, J. Knoska, S. Schon, T. Sato, M. S. Hunter, A. Hosseinizadeh, C. Kuptiz, R. Nazari, R. C. Alvarez, K. Karpos, S. Zaare, Z. Dobson, E. Discianno, S. Zhang, J. D. Zook, J. Bielecki, R. de Wijn, A. R. Round, P. Vagovic, M. Kloos, M. Vakili, G. K. Ketawala, N. E. Stander, T. L. Olson, K. Morin, J. Mondal, J. Nguyen, J. D. Meza-Aguilar, G. Kodis, S. Vaiana, J. M. Martin-Garcia, V. Mariani, P. Schwander, M. Schmidt, M. Messerschmidt, A. Ourmazd, N. Zatsepin, U. Weierstall, B. D. Bruce, A. P. Mancuso, T. Grant, A. Barty, H. N. Chapman, M. Frank, R. Fromme, J. C. H. Spence, S. Botha,

P. Fromme, R. A. Kirian and A. Ros, *J. Appl. Crystallogr.*, 2022, **55**, 1–13.

31 M. Sugahara, E. Mizohata, E. Nango, M. Suzuki, T. Tanaka, T. Masuda, R. Tanaka, T. Shimamura, Y. Tanaka, C. Suno, K. Ihara, D. Pan, K. Kakinouchi, S. Sugiyama, M. Murata, T. Inoue, K. Tono, C. Song, J. Park, T. Kameshima, T. Hatsui, Y. Joti, M. Yabashi and S. Iwata, *Nat. Methods*, 2014, **12**, 61.

32 M. Sugahara, C. Song, M. Suzuki, T. Masuda, S. Inoue, T. Nakane, F. Yumoto, E. Nango, R. Tanaka, K. Tono, Y. Joti, T. Kameshima, T. Hatsui, M. Yabashi, O. Nureki, K. Numata and S. Iwata, *Sci. Rep.*, 2016, **6**, 24484.

33 U. Weierstall, D. James, C. Wang, T. A. White, D. Wang, W. Liu, J. C. Spence, R. Bruce Doak, G. Nelson, P. Fromme, R. Fromme, I. Grotjohann, C. Kupitz, N. A. Zatsepin, H. Liu, S. Basu, D. Wacker, G. W. Han, V. Katritch, S. Boutet, M. Messerschmidt, G. J. Williams, J. E. Koglin, M. Marvin Seibert, M. Klinker, C. Gati, R. L. Shoeman, A. Barty, H. N. Chapman, R. A. Kirian, K. R. Beyerlein, R. C. Stevens, D. Li, S. T. Shah, N. Howe, M. Caffrey and V. Cherezov, *Nat. Commun.*, 2014, **5**, 3309.

34 W. Liu, D. Wacker, C. Wang, E. Abola and V. Cherezov, *Philos. Trans. R. Soc., B*, 2014, **369**, 20130314.

35 R. G. Sierra, H. Laksmono, J. Kern, R. Tran, J. Hattne, R. Alonso-Mori, B. Lassalle-Kaiser, C. Glöckner, J. Hellmich, D. W. Schafer, N. Echols, R. J. Gildea, R. W. Grosse-Kunstleve, J. Sellberg, T. A. McQueen, A. R. Fry, M. M. Messerschmidt, A. Miahnahri, M. M. Seibert, C. Y. Hampton, D. Starodub, N. D. Loh, D. Sokaras, T.-C. Weng, P. H. Zwart, P. Glatzel, D. Milathianaki, W. E. White, P. D. Adams, G. J. Williams, S. Boutet, A. Zouni, J. Messinger, N. K. Sauter, U. Bergmann, J. Yano, V. K. Yachandra and M. J. Bogan, *Acta Crystallogr., Sect. D: Biol. Crystallogr.*, 2012, **68**, 1584–1587.

36 R. G. Sierra, C. Gati, H. Laksmono, E. H. Dao, S. Gul, F. Fuller, J. Kern, R. Chatterjee, M. Ibrahim, A. S. Brewster, I. D. Young, T. Michels-Clark, A. Aquila, M. Liang, M. S. Hunter, J. E. Koglin, S. Boutet, E. A. Junco, B. Hayes, M. J. Bogan, C. Y. Hampton, E. V. Puglisi, N. K. Sauter, C. A. Stan, A. Zouni, J. Yano, V. K. Yachandra, S. M. Soltis, J. D. Puglisi and H. DeMirci, *Nat. Methods*, 2016, **13**, 59–62.

37 R. J. Jernigan, D. Logeswaran, D. Doppler, N. Nagaratnam, M. Sonker, J.-H. Yang, G. Ketawala, J. M. Martin-Garcia, M. L. Shelby, T. D. Grant, V. Mariani, A. Tolstikova, M. Z. Sheikh, M. C. Yung, M. A. Coleman, S. Zaare, E. K. Kaschner, M. T. Rabbani, R. Nazari, M. A. Zacks, B. Hayes, R. G. Sierra, M. S. Hunter, S. Lisova, A. Batyuk, C. Kupitz, S. Boutet, D. T. Hansen, R. A. Kirian, M. Schmidt, R. Fromme, M. Frank, A. Ros, J. J. L. Chen, S. Botha and P. Fromme, *Structure*, 2023, **31**, 138–151.e5.

38 P. Roedig, H. M. Ginn, T. Pakendorf, G. Sutton, K. Harlos, T. S. Walter, J. Meyer, P. Fischer, R. Duman, I. Vartiainen, B. Reime, M. Warmer, A. S. Brewster, I. D. Young, T. Michels-Clark, N. K. Sauter, A. Kotecha, J. Kelly, D. J. Rowlands, M. Sikorsky, S. Nelson, D. S. Damiani, R. Alonso-Mori, J. Ren, E. E. Fry, C. David, D. I. Stuart, A. Wagner and A. Meents, *Nat. Methods*, 2017, **14**, 805–810.

39 J. M. Lahey-Rudolph, R. Schonherr, M. Barthelmess, P. Fischer, C. Seuring, A. Wagner, A. Meents and L. Redecke, *IUCrJ*, 2021, **8**, 665–677.

40 A. Karpik, I. Martiel, P. M. Kristiansen and C. Padeste, *Micro Nano Eng.*, 2020, **7**, 100053.

41 M. Denz, G. Brehm, C. Y. J. Hemonnot, H. Spears, A. Wittmeier, C. Cassini, O. Saldanha, E. Perego, A. Diaz, M. Burghammer and S. Koster, *Lab Chip*, 2017, **18**, 171–178.

42 A. Y. Lyubimov, T. D. Murray, A. Koehl, I. E. Araci, M. Uervirojnangkoorn, O. B. Zeldin, A. E. Cohen, S. M. Soltis, E. L. Baxter, A. S. Brewster, N. K. Sauter, A. T. Brunger and J. M. Berger, *Acta Crystallogr., Sect. D: Biol. Crystallogr.*, 2015, **71**, 928–940.

43 J. M. Schieferstein, A. S. Pawate, M. J. Varel, S. Guha, I. Astrauskaite, R. B. Gennis and P. J. A. Kenis, *Lab Chip*, 2018, **18**, 944–954.

44 R. B. Doak, G. Nass Kovacs, A. Gorel, L. Foucar, T. R. M. Barends, M. L. Grunbein, M. Hilpert, M. Kloos, C. M. Roome, R. L. Shoeman, M. Stricker, K. Tono, D. You, K. Ueda, D. A. Sherrell, R. L. Owen and I. Schlichting, *Acta Crystallogr., Sect. D: Struct. Biol.*, 2018, **74**, 1000–1007.

45 M. L. Shelby, D. Gilbile, T. D. Grant, C. Seuring, B. W. Segelke, W. He, A. C. Evans, T. Pakendorf, P. Fischer, M. S. Hunter, A. Batyuk, M. Barthelmess, A. Meents, M. A. Coleman, T. L. Kuhl and M. Frank, *IUCrJ*, 2020, **7**, 30–41.

46 D. Lee, S. Park, K. Lee, J. Kim, G. Park, K. H. Nam, S. Baek, W. K. Chung, J.-L. Lee, Y. Cho and J. Park, *J. Appl. Crystallogr.*, 2020, **53**, 477–485.

47 A. Echelmeier, M. Sonker and A. Ros, *Anal. Bioanal. Chem.*, 2019, **411**, 6535–6547.

48 M. S. Hunter, B. Segelke, M. Messerschmidt, G. J. Williams, N. A. Zatsepin, A. Barty, W. H. Benner, D. B. Carlson, M. Coleman, A. Graf, S. P. Hau-Riege, T. Pardini, M. M. Seibert, J. Evans, S. Boutet and M. Frank, *Sci. Rep.*, 2014, **4**, 6026.

49 S. Oghbaey, A. Sarracini, H. M. Ginn, O. Pare-Labrosse, A. Kuo, A. Marx, S. W. Epp, D. A. Sherrell, B. T. Eger, Y. Zhong, R. Loch, V. Mariani, R. Alonso-Mori, S. Nelson, H. T. Lemke, R. L. Owen, A. R. Pearson, D. I. Stuart, O. P. Ernst, H. M. Mueller-Werkmeister and R. J. Miller, *Acta Crystallogr., Sect. D: Struct. Biol.*, 2016, **72**, 944–955.

50 C. Mueller, A. Marx, S. W. Epp, Y. Zhong, A. Kuo, A. R. Balo, J. Soman, F. Schotte, H. T. Lemke, R. L. Owen, E. F. Pai, A. R. Pearson, J. S. Olson, P. A. Anfinrud, O. P. Ernst and R. J. Dwayne Miller, *Struct. Dyn.*, 2015, **2**, 054302.

51 F. Mafune, K. Miyajima, K. Tono, Y. Takeda, J. Y. Kohno, N. Miyauchi, J. Kobayashi, Y. Joti, E. Nango, S. Iwata and M. Yabashi, *Acta Crystallogr., Sect. D: Struct. Biol.*, 2016, **72**, 520–523.

52 C. G. Roessler, R. Agarwal, M. Allaire, R. Alonso-Mori, B. Andi, J. F. R. Bachega, M. Bommer, A. S. Brewster, M. C. Browne, R. Chatterjee, E. Cho, A. E. Cohen, M. Cowan, S. Datwani, V. L. Davidson, J. Defever, B. Eaton, R. Ellson, Y. Feng, L. P. Ghislain, J. M. Glownia, G. Han, J. Hattne, J. Hellmich, A. Heroux, M. Ibrahim, J. Kern, A. Kuczewski, H. T. Lemke, P. Liu, L. Majlof, W. M. McClintock, S. Myers, S. Nelsen, J. Olechno, A. M. Orville, N. K. Sauter, A. S.

Soares, S. M. Soltis, H. Song, R. G. Stearns, R. Tran, Y. Tsai, M. Uervirojnangkoorn, C. M. Wilmot, V. Yachandra, J. Yano, E. T. Yukl, D. Zhu and A. Zouni, *Structure*, 2016, **24**, 631–640.

53 F. D. Fuller, S. Gul, R. Chatterjee, E. S. Burgie, I. D. Young, H. Lebrette, V. Srinivas, A. S. Brewster, T. Michels-Clark, J. A. Clinger, B. Andi, M. Ibrahim, E. Pastor, C. de Lichtenberg, R. Hussein, C. J. Pollock, M. Zhang, C. A. Stan, T. Kroll, T. Fransson, C. Weninger, M. Kubin, P. Aller, L. Lassalle, P. Brauer, M. D. Miller, M. Amin, S. Koroidov, C. G. Roessler, M. Allaire, R. G. Sierra, P. T. Docker, J. M. Glownia, S. Nelson, J. E. Koglin, D. L. Zhu, M. Chollet, S. Song, H. Lemke, M. N. Liang, D. Sokaras, R. Alonso-Mori, A. Zouni, J. Messinger, U. Bergmann, A. K. Boal, J. M. Bollinger, C. Krebs, M. Hogbom, G. N. Phillips, R. D. Vierstra, N. K. Sauter, A. M. Orville, J. Kern, V. K. Yachandra and J. Yano, *Nat. Methods*, 2017, **14**, 443–449.

54 R. Cheng, *Crystals*, 2020, **10**, 215.

55 D. Kim, A. Echelmeier, J. Cruz Villarreal, S. Gandhi, S. Quintana, A. Egatz-Gomez and A. Ros, *Anal. Chem.*, 2019, **91**, 9792–9799.

56 A. Echelmeier, D. Kim, J. Cruz Villarreal, J. Coe, S. Quintana, G. Brehm, A. Egatz-Gomez, R. Nazari, R. G. Sierra, J. E. Koglin, A. Batyuk, M. S. Hunter, S. Boutet, N. Zatsepin, R. A. Kirian, T. D. Grant, P. Fromme and A. Ros, *J. Appl. Crystallogr.*, 2019, **52**, 997–1008.

57 A. Echelmeier, J. Cruz Villarreal, M. Messerschmidt, D. Kim, J. D. Coe, D. Thifault, S. Botha, A. Egatz-Gomez, S. Gandhi, G. Brehm, C. E. Conrad, D. T. Hansen, C. Madsen, S. Bajt, J. D. Meza-Aguilar, D. Oberthür, M. O. Wiedorn, H. Fleckenstein, D. Mendez, J. Knoška, J. M. Martin-Garcia, H. Hu, S. Lisova, A. Allahgholi, Y. Gevorkov, K. Ayyer, S. Aplin, H. M. Ginn, H. Graafsma, A. J. Morgan, D. Greiffenberg, A. Klujev, T. Laurus, J. Poehlsen, U. Trunk, D. Mezza, B. Schmidt, M. Kuhn, R. Fromme, J. Sztuk-Dambietz, N. Raab, S. Hauf, A. Silenzi, T. Michelat, C. Xu, C. Danilevski, A. Parenti, L. Mekinda, B. Weinhausen, G. Mills, P. Vagovic, Y. Kim, H. Kirkwood, R. Bean, J. Bielecki, S. Stern, K. Giewekemeyer, A. R. Round, J. Schulz, K. Dörner, T. D. Grant, V. Mariani, A. Barty, A. P. Mancuso, U. Weierstall, J. C. H. Spence, H. N. Chapman, N. Zatsepin, P. Fromme, R. A. Kirian and A. Ros, *Nat. Commun.*, 2020, **11**, 4511.

58 M. Sonker, D. Doppler, A. Egatz-Gomez, S. Zaare, M. T. Rabbani, A. Manna, J. Cruz Villarreal, G. Nelson, G. K. Ketawala, K. Karpos, R. C. Alvarez, R. Nazari, D. Thifault, R. Jernigan, D. Oberthür, H. Han, R. Sierra, M. S. Hunter, A. Batyuk, C. J. Kupitz, R. E. Sublett, F. Poitevin, S. Lisova, V. Mariani, A. Tolstikova, S. Boutet, M. Messerschmidt, J. D. Meza-Aguilar, R. Fromme, J. M. Martin-Garcia, S. Botha, P. Fromme, T. D. Grant, R. A. Kirian and A. Ros, *Biophys. Rep.*, 2022, **2**(4), 100081.

59 A. L. Pey, C. F. Megarity, E. Medina-Carmona and D. J. Timson, *Curr. Drug Targets*, 2016, **17**, 1506–1514.

60 E. Salido, D. J. Timson, I. Betancor-Fernandez, R. Palomino-Morales, E. Anoz-Carbonell, J. L. Pacheco-Garcia, M. Medina and A. L. Pey, *J. Pers. Med.*, 2022, **12**(5), 747.

61 D. Ross and D. Siegel, *Front. Physiol.*, 2017, **8**, 595.

62 S. Beaver, N. Mesa-Torres, A. L. Pey and D. J. Timson, *Biochim. Biophys. Acta, Proteins Proteomics*, 2019, **1867**, 663–676.

63 R. Nazari, S. Zaare, R. C. Alvarez, K. Karpos, T. Engelman, C. Madsen, G. Nelson, J. C. H. Spence, U. Weierstall, R. J. Adrian and R. A. Kirian, *Opt. Express*, 2020, **28**, 21749–21765.

64 G. Nelson, R. A. Kirian, U. Weierstall, N. A. Zatsepin, T. Farago, T. Baumbach, F. Wilde, F. B. Niesler, B. Zimmer, I. Ishigami, M. Hikita, S. Bajt, S. R. Yeh, D. L. Rousseau, H. N. Chapman, J. C. Spence and M. Heymann, *Opt. Express*, 2016, **24**, 11515–11530.

65 L. Lomb, J. Steinbrener, S. Bari, D. Beisel, D. Berndt, C. Kieser, M. Lukat, N. Neef and R. L. Shoeman, *J. Appl. Crystallogr.*, 2012, **45**, 674–678.

66 C. Gisriel, J. Coe, R. Letrun, O. M. Yefanov, C. Luna-Chavez, N. E. Stander, S. Lisova, V. Mariani, M. Kuhn, S. Aplin, T. D. Grant, K. Dorner, T. Sato, A. Echelmeier, J. Cruz Villarreal, M. S. Hunter, M. O. Wiedorn, J. Knoska, V. Mazalova, S. Roy-Chowdhury, J. H. Yang, A. Jones, R. Bean, J. Bielecki, Y. Kim, G. Mills, B. Weinhausen, J. D. Meza, N. Al-Qudami, S. Bajt, G. Brehm, S. Botha, D. Boukhelef, S. Brockhauser, B. D. Bruce, M. A. Coleman, C. Danilevski, E. Discianno, Z. Dobson, H. Fangohr, J. M. Martin-Garcia, Y. Gevorkov, S. Hauf, A. Hosseinizadeh, F. Januschek, G. K. Ketawala, C. Kupitz, L. Maia, M. Manetti, M. Messerschmidt, T. Michelat, J. Mondal, A. Ourmazd, G. Previtali, I. Sarrou, S. Schon, P. Schwander, M. L. Shelby, A. Silenzi, J. Sztuk-Dambietz, J. Szuba, M. Turcato, T. A. White, K. Wrona, C. Xu, M. H. Abdellatif, J. D. Zook, J. C. H. Spence, H. N. Chapman, A. Barty, R. A. Kirian, M. Frank, A. Ros, M. Schmidt, R. Fromme, A. P. Mancuso, P. Fromme and N. A. Zatsepin, *Nat. Commun.*, 2019, **10**, 5021.

67 A. L. Pey, C. F. Megarity and D. J. Timson, *Biochim. Biophys. Acta*, 2014, **1842**, 2163–2173.

68 C. Kupitz, I. Grotjohann, C. E. Conrad, S. Roy-Chowdhury, R. Fromme and P. Fromme, *Philos. Trans. R. Soc. London, Ser. B*, 2014, **369**, 20130316.

69 E. Medina-Carmona, J. E. Fuchs, J. A. Gavira, N. Mesa-Torres, J. L. Neira, E. Salido, R. Palomino-Morales, M. Burgos, D. J. Timson and A. L. Pey, *Hum. Mol. Genet.*, 2017, **26**(18), 3531–3544.

70 T. B. Van Driel, S. Nelson, R. Armenta, G. Blaj, S. Boo, S. Boutet, D. Doering, A. Dragone, P. Hart, G. Haller, C. Kenney, M. Kwaitowski, L. Manger, M. McKelvey, K. Nakahara, M. Oriunno, T. Sato and M. Weaver, *J. Synchrotron Radiat.*, 2020, **27**, 608–615.

71 V. Mariani, A. Morgan, C. H. Yoon, T. J. Lane, T. A. White, C. O'Grady, M. Kuhn, S. Aplin, J. Koglin, A. Barty and H. N. Chapman, *J. Appl. Crystallogr.*, 2016, **49**, 1073–1080.

72 A. Barty, R. A. Kirian, F. R. Maia, M. Hantke, C. H. Yoon, T. A. White and H. Chapman, *J. Appl. Crystallogr.*, 2014, **47**, 1118–1131.

73 T. A. White, R. A. Kirian, A. V. Martin, A. Aquila, K. Nass, A. Barty and H. N. Chapman, *J. Appl. Crystallogr.*, 2012, **45**, 335–341.

74 Y. Gevorkov, O. Yefanov, A. Barty, T. A. White, V. Mariani, W. Brehm, A. Tolstikova, R. R. Grigat and H. N. Chapman, *Acta Crystallogr., Sect. A: Found. Adv.*, 2019, **75**, 694–704.
75 T. G. G. Battye, L. Kontogiannis, O. Johnson, H. R. Powell and A. G. W. Leslie, *Acta Crystallogr., Sect. D: Biol. Crystallogr.*, 2011, **67**, 271–281.
76 A. Duisenberg, *J. Appl. Crystallogr.*, 1992, **25**, 92–96.
77 M. D. Winn, C. C. Ballard, K. D. Cowtan, E. J. Dodson, P. Emsley, P. R. Evans, R. M. Keegan, E. B. Krissinel, A. G. Leslie, A. McCoy, S. J. McNicholas, G. N. Murshudov, N. S. Pannu, E. A. Potterton, H. R. Powell, R. J. Read, A. Vagin and K. S. Wilson, *Acta Crystallogr., Sect. D: Biol. Crystallogr.*, 2011, **67**, 235–242.
78 A. J. McCoy, R. W. Grosse-Kunstleve, P. D. Adams, M. D. Winn, L. C. Storoni and R. J. Read, *J. Appl. Crystallogr.*, 2007, **40**, 658–674.
79 M. Faig, M. A. Bianchet, P. Talalay, S. Chen, S. Winski, D. Ross and L. M. Amzel, *Proc. Natl. Acad. Sci. U. S. A.*, 2000, **97**, 3177–3182.
80 G. N. Murshudov, P. Skubak, A. A. Lebedev, N. S. Pannu, R. A. Steiner, R. A. Nicholls, M. D. Winn, F. Long and A. A. Vagin, *Acta Crystallogr., Sect. D: Biol. Crystallogr.*, 2011, **67**, 355–367.
81 P. Emsley, B. Lohkamp, W. G. Scott and K. Cowtan, *Acta Crystallogr., Sect. D: Biol. Crystallogr.*, 2010, **66**, 486–501.
82 J. M. Martin-Garcia, S. Botha, H. Hu, R. Jernigan, A. Castellvi, S. Lisova, F. Gil, B. Calisto, I. Crespo, S. Roy-Chowdhury, A. Grieco, G. Ketawala, U. Weierstall, J. Spence, P. Fromme, N. Zatsepin, D. R. Boer and X. Carpena, *J. Synchrotron Radiat.*, 2022, **29**, 1130.
83 L. L. C. Schroedinger, *PyMOL Molecular Graphics System*, 2020.
84 W. D. Lienhart, E. Strandback, V. Gudipati, K. Koch, A. Binter, M. K. Uhl, D. M. Rantasa, B. Bourgeois, T. Madl, K. Zangger, K. Gruber and P. Macheroux, *FEBS J.*, 2017, **284**, 1233–1245.
85 L. S. Pidugu, J. C. Mbimba, M. Ahmad, E. Pozharski, E. A. Sausville, A. Emadi and E. A. Toth, *BMC Struct. Biol.*, 2016, **16**, 1.
86 W. Liu, D. Wacker, C. Gati, G. W. Han, D. James, D. Wang, G. Nelson, U. Weierstall, V. Katritch, A. Barty, N. A. Zatsepin, D. Li, M. Messerschmidt, S. Boutet, G. J. Williams, J. E. Koglin, M. M. Seibert, C. Wang, S. T. Shah, S. Basu, R. Fromme, C. Kupitz, K. N. Rendek, I. Grotjohann, P. Fromme, R. A. Kirian, K. R. Beyerlein, T. A. White, H. N. Chapman, M. Caffrey, J. C. Spence, R. C. Stevens and V. Cherezov, *Science*, 2013, **342**, 1521–1524.
87 D. Pan, R. Oyama, T. Sato, T. Nakane, R. Mizunuma, K. Matsuoka, Y. Joti, K. Tono, E. Nango, S. Iwata, T. Nakatsu and H. Kato, *IUCrJ*, 2022, **9**, 134–145.
88 E. Ayan, B. Yuksel, E. Destan, F. B. Ertem, G. Yildirim, M. Eren, O. M. Yefanov, A. Barty, A. Tolstikova, G. K. Ketawala, S. Botha, E. H. Dao, B. Hayes, M. Liang, M. H. Seaberg, M. S. Hunter, A. Batyuk, V. Mariani, Z. Su, F. Poitevin, C. H. Yoon, C. Kupitz, A. Cohen, T. Doukov, R. G. Sierra, C. Dag and H. DeMirci, *Commun. Biol.*, 2022, **5**, 73.
89 A. M. Wolff, I. D. Young, R. G. Sierra, A. S. Brewster, M. W. Martynowycz, E. Nango, M. Sugahara, T. Nakane, K. Ito, A. Aquila, A. Bhowmick, J. T. Biel, S. Carbajo, A. E. Cohen, S. Cortez, A. Gonzalez, T. Hino, D. Im, J. D. Koralek, M. Kubo, T. S. Lazarou, T. Nomura, S. Owada, A. J. Samelson, T. Tanaka, R. Tanaka, E. M. Thompson, H. van den Bedem, R. A. Woldeyes, F. Yumoto, W. Zhao, K. Tono, S. Boutet, S. Iwata, T. Gonen, N. K. Sauter, J. S. Fraser and M. C. Thompson, *IUCrJ*, 2020, **7**, 306–323.
90 V. Srinivas, R. Banerjee, H. Lebrette, J. C. Jones, O. Aurelius, I. S. Kim, C. C. Pham, S. Gul, K. D. Sutherlin, A. Bhowmick, J. John, E. Bozkurt, T. Fransson, P. Aller, A. Butryn, I. Bogacz, P. Simon, S. Keable, A. Britz, K. Tono, K. S. Kim, S. Y. Park, S. J. Lee, J. Park, R. Alonso-Mori, F. D. Fuller, A. Batyuk, A. S. Brewster, U. Bergmann, N. K. Sauter, A. M. Orville, V. K. Yachandra, J. Yano, J. D. Lipscomb, J. Kern and M. Hogbom, *J. Am. Chem. Soc.*, 2020, **142**, 14249–14266.
91 R. Suno, K. T. Kimura, T. Nakane, K. Yamashita, J. Wang, T. Fujiwara, Y. Yamanaka, D. Im, S. Horita, H. Tsujimoto, M. S. Tawaramoto, T. Hirokawa, E. Nango, K. Tono, T. Kameshima, T. Hatsui, Y. Joti, M. Yabashi, K. Shimamoto, M. Yamamoto, D. M. Rosenbaum, S. Iwata, T. Shimamura and T. Kobayashi, *Structure*, 2018, **26**, 7–19, e15.
92 G. Fenalti, N. A. Zatsepin, C. Betti, P. Giguere, G. W. Han, A. Ishchenko, W. Liu, K. Guillemyn, H. Zhang, D. James, D. Wang, U. Weierstall, J. C. Spence, S. Boutet, M. Messerschmidt, G. J. Williams, C. Gati, O. M. Yefanov, T. A. White, D. Oberthuer, M. Metz, C. H. Yoon, A. Barty, H. N. Chapman, S. Basu, J. Coe, C. E. Conrad, R. Fromme, P. Fromme, D. Tourwe, P. W. Schiller, B. L. Roth, S. Ballet, V. Katritch, R. C. Stevens and V. Cherezov, *Nat. Struct. Mol. Biol.*, 2015, **22**, 265–268.
93 T. Mehlman, J. Biel, S. M. Azeem, E. Nelson, S. Hossain, L. Dunnett, N. Paterson, A. Douangamath, R. Talon, D. Axford, H. Orins, F. Delft and D. Keedy, *eLife*, 2023, **12**, e84632.
94 R. Li, M. Blianchet, P. Talalay and L. M. Amzel, *Proc. Natl. Acad. Sci. U. S. A.*, 1995, **92**, 8846–8850.
95 G. Asher, O. Dym, P. Tsvetkov, J. Adler and Y. Shaul, *Biochemistry*, 2006, **45**, 6372–6378.
96 Q. Ma, K. Cui, F. Xiao, A. Y. Lu and C. S. Yang, *J. Biol. Chem.*, 1992, **267**, 22298–22304.
97 P. Pandey, B. Avula, I. A. Khan, S. I. Khan, V. J. Navarro, R. J. Doerksen and A. G. Chittiboyina, *Chem. Res. Toxicol.*, 2020, **33**, 2749–2764.
98 C. F. Megarity, H. Abdel-Aal Bettley, M. C. Caraher, K. A. Scott, R. C. Whitehead, T. A. Jowitt, A. Gutierrez, R. A. Bryce, K. A. Nolan, I. J. Stratford and D. J. Timson, *ChemBioChem*, 2019, **20**, 2841–2849.
99 P. Vankova, E. Salido, D. J. Timson, P. Man and A. L. Pey, *Biomolecules*, 2019, **9**(11), 728.
100 E. Anoz-Carbonell, D. J. Timson, A. L. Pey and M. Medina, *Antioxidants*, 2020, **9**(9), 772.
101 J. L. Pacheco-Garcia, E. Anoz-Carbonell, P. Vankova, A. Kannan, R. Palomino-Morales, N. Mesa-Torres, E. Salido, P.

Man, M. Medina, A. N. Naganathan and A. L. Pey, *Redox Biol.*, 2021, **46**, 102112.

102 S. Vega, O. Abian and A. Velazquez-Campoy, *Biochim. Biophys. Acta*, 2016, **1860**, 868–878.